Supporting Information

Effects of Ethanol (E85) Versus Gasoline Vehicles on Cancer and Mortality in the United States

Mark Z. Jacobson*

*Department of Civil and Environmental Engineering, Stanford University, Stanford, California 94305-4020, USA. Tel: 650-723-6836. Email: jacobson@stanford.edu

Environmental Science & Technology

Summary
This Supporting Information describes the model used for this study (Section 1), discusses emissions data and initialization (Section 2), and discusses, and analyzes simulation and health-effects results additional to those discussed in the main paper (Section 3). Section 3.C. provides cancer risk information and Section 3.D provides ozone health risk information.

1. Description of the Model

The model used for this study was GATOR-GCMOM, a parallelized and one-way-nested global-through-urban scale Gas, Aerosol, Transport, Radiation, General Circulation, Mesoscale, and Ocean Model (*S1-S12*). The model treated time-dependent gas, aerosol, cloud, radiative, dynamical, ocean, and transport processes. Aerosol processes were treated among a single aerosol size distribution with multiple components per size bin. Cloud processes were treated among three hydrometeor size distributions (liquid, ice, graupel), each containing aerosol inclusions. Size-resolved aerosols, clouds, and their chemical inclusions were transported in 3-D. All processes described were solved in all grid cells in the stratosphere and troposphere. The model was parallelized with Message Passing Interface (MPI). The model has been compared with paired-in-time-and-space data for meteorological, gas, aerosol, and/or radiative parameters in several studies, including those in the Los Angeles basin (*S1, S3, S7, S12*) and the U.S. as a whole (*S9, S11*), which are the domains considered here. Thus, further comparisons with data were not performed here.

1.A. Atmospheric Dynamical and Transport Processes

On the global scale, the model solved the momentum equation under the hydrostatic assumption and the thermodynamic energy equation with a potential-enstrophy, mass, and energy-conserving scheme (*S13*). In nested regional domains, the dynamical solution scheme conserved enstrophy, mass, and kinetic energy (*S14*). Dynamical schemes on all domains used spherical and sigma-pressure coordinates in the horizontal and vertical, respectively. Transport of gases (including water vapor) and aerosol particles was solved with a conservative, monotonic method (*S15*) using modeled online winds and vertical diffusion coefficients.

1.B. Gas processes

Gas processes included emission, photochemistry, advection, turbulence, cloud convection of gases, nucleation, washout, dry deposition, and condensation onto and dissolution into aerosol particles, clouds, and precipitation. Gases affected solar and thermal-IR radiation, aerosol formation, and cloud evolution, all of which fed back to meteorology. Gas photochemistry was solved with SMVGEAR II (*S16*). The gas-phase chemical mechanism for this study included 126 gases, 263 kinetic reactions, and 36 photolysis reactions solved in all model domains (Table S1).

Table S1. Gas-phase chemical kinetic reactions, reaction rate coefficients, and photoprocesses treated in all model domains here.

No.	Kinetic Reaction	F_c [a]	Rate Coefficient (s^{-1}, $cm^3\ s^{-1}$, or $cm^6\ s^{-1}$)	Ref.[b]
	Inorganic Chemistry			
1	$O + O_2 + M \rightarrow O_3 + M$		$6.00\times10^{-34}\ (300/T)^{2.3}$	A
2	$O + O_3 \rightarrow 2\ O_2$		$8.00\times10^{-12}\ e^{-2060/T}$	A
3	$O(^1D) + O_3 \rightarrow 2O_2$		1.20×10^{-10}	A
4	$O(^1D) + O_3 \rightarrow O_2 + 2O$		1.20×10^{-10}	A
5	$O(^1D) + O_2 \rightarrow O + O_2$		$3.30\times10^{-11}\ e^{55/T}$	A
6	$O(^1D) + N_2 \rightarrow O + N_2$		$2.15\times10^{-11}\ e^{110/T}$	A
7	$O(^1D) + CO_2 \rightarrow O + CO_2$		$7.50\times10^{-11}\ e^{115/T}$	A
8	$O(^1D) + N_2 + M \rightarrow N_2O + M$		$2.80\times10^{-36}\ (300/T)^{0.9}$	A

9	$O(^1D) + N_2O \rightarrow N_2 + O_2$		$4.90\times10^{-11}\ e^{20/T}$	A
10	$O(^1D) + N_2O \rightarrow NO + NO$		$6.70\times10^{-11}\ e^{20/T}$	A
11	$O(^1D) + H_2 \rightarrow OH + H$		1.10×10^{-10}	A
12	$O(^1D) + H_2O \rightarrow OH + OH$		$1.63\times10^{-10}\ e^{60/T}$	A
13	$H + O_2 \xrightarrow{M} HO_2$	(P) 0.6	$4.40\times10^{-32}\ (300/T)^{1.3}$ $4.70\times10^{-11}\ (300/T)^{0.2}$	A
14	$H + O_3 \rightarrow O_2 + OH$		$1.40\times10^{-10}\ e^{-470/T}$	A
15	$H + HO_2 \rightarrow H_2 + O_2$		5.67×10^{-12}	A
16	$H + HO_2 \rightarrow OH + OH$		7.29×10^{-11}	A
17	$H + HO_2 \rightarrow H_2O + O$		2.43×10^{-12}	A
18	$OH + O \rightarrow H + O_2$		$2.20\times10^{-11}\ e^{120/T}$	A
19	$OH + O_3 \rightarrow HO_2 + O_2$		$1.70\times10^{-12}\ e^{-940/T}$	A
20	$OH + H_2 \rightarrow H_2O + H$		$2.8\times10^{-12}\ e^{-1800/T}$	A
21	$OH + OH \rightarrow H_2O + O$		$1{,}80\times10^{-12}$	A
22	$OH + OH \xrightarrow{M} H_2O_2$	(P) 0.6	$6.90\times10^{-31}\ (300/T)^{0.8}$ 2.6×10^{-11}	A
23	$OH + HO_2 \rightarrow H_2O + O_2$		$4.80\times10^{-11}\ e^{250/T}$	A
24	$OH + H_2O_2 \rightarrow HO_2 + H_2O$		1.80×10^{-12}	A
25	$OH + NO \xrightarrow{M} HONO$	(P) 0.6	$7.00\times10^{-31}\ (300/T)^{2.6}$ $3.60\times10^{-11}\ (300/T)^{0.1}$	A
26	$OH + NO_2 \xrightarrow{M} HNO_3$	(P) 0.6	$1.80\times10^{-30}\ (300/T)^{3.0}$ 2.80×10^{-11}	A
27	$OH + NO_3 \rightarrow HO_2 + NO_2$		2.20×10^{-11}	A
28	$OH + HONO \rightarrow H_2O + NO_2$		$1.80\times10^{-11}\ e^{-390/T}$	A
29	$OH + HNO_3 \rightarrow H_2O + NO_3$		c	A
30	$OH + HO_2NO_2 \rightarrow H_2O + NO_2 + O_2$		$1.30\times10^{-12}\ e^{380/T}$	A
31	$OH + CO \rightarrow HO_2 + CO_2$		d	A
32	$HO_2 + O \rightarrow OH + O_2$		$3.00\times10^{-11}\ e^{200/T}$	A
33	$HO_2 + O_3 \rightarrow OH + 2O_2$		$1.40\times10^{-14}\ e^{-490/T}$	A
34	$HO_2 + HO_2 \rightarrow H_2O_2 + O_2$		e	A
35	$HO_2 + NO \rightarrow OH + NO_2$		$3.50\times10^{-12}\ e^{250/T}$	A
36	$HO_2 + NO_2 \xrightarrow{M} HO_2NO_2$	(P) 0.6	$2.00\times10^{-31}\ (300/T)^{3.4}$ $2.90\times10^{-12}\ (300/T)^{1.1}$	A
37	$HO_2NO_2 \xrightarrow{M} HO_2 + NO_2$		$k_{36} / (2.10\times10^{-27} \times e^{10900/T})$	
38	$HO_2 + NO_3 \rightarrow HNO_3 + O_2$		3.50×10^{-12}	A
39	$H_2O_2 + O \rightarrow OH + HO_2$		$1.40\times10^{-12}\ e^{-2000/T}$	A
40	$NO + O \xrightarrow{M} NO_2$	(P) 0.6	$9.00\times10^{-32}\ (300/T)^{1.5}$ 3.00×10^{-11}	A
41	$NO + O_3 \rightarrow NO_2 + O_2$		$3.00\times10^{-12} e^{-1500/T}$	A
42	$NO_2 + O \rightarrow NO + O_2$		$5.60\times10^{-12} e^{180/T}$	A
43	$NO_2 + O \xrightarrow{M} NO_3$	(P) 0.6	$2.50\times10^{-31}\ (300/T)^{1.8}$ $2.20\times10^{-11}\ (300/T)^{0.7}$	A
44	$NO_2 + O_3 \rightarrow NO_3 + O_2$		$1.20\times10^{-13}\ e^{-2450/T}$	A
45	$NO_3 + O \rightarrow NO_2 + O_2$		1.00×10^{-11}	A
46	$NO_3 + NO \rightarrow 2\ NO_2$		$1.50\times10^{-11}\ e^{170/T}$	B
47	$NO_3 + NO_2 \xrightarrow{M} N_2O_5$	(P) 0.6	$2.00\times10^{-30}\ (300/T)^{4.4}$	A

			$1.40 \times 10^{-12} (300/T)^{0.7}$	
48	$N_2O_5 \xrightarrow{M} NO_3 + NO_2$		$K_{47} / (3.00 \times 10^{-27} \times e^{10990/T})$	A
49	$N_2O_5 + H_2O \rightarrow 2\ HNO_3$		2.00×10^{-21}	B
	Organic Chemistry			
	Alkane, Alkene, and Aldehyde Chemistry			
50	$CH_4 + O(^1D) \rightarrow CH_3O_2 + OH$		1.50×10^{-10}	A
51	$CH_4 + O(^1D) \rightarrow CH_3O + H$		3.00×10^{-11}	B
52	$CH_4 + O(^1D) \rightarrow HCHO + H_2$		7.00×10^{-12}	B
53	$CH_4 + OH \rightarrow CH_3O_2 + H_2O$		$2.45 \times 10^{-12} e^{-1775/T}$	A
54	$CH_3O + O_2 \rightarrow HCHO + HO_2$		$3.90 \times 10^{-14} e^{-900/T}$	A
55	$CH_3O + NO \rightarrow HCHO + HO_2 + NO$		8.00×10^{-12}	A
56	$CH_3O + NO \xrightarrow{M} CH_3ONO$	(P) 0.6	$2.30 \times 10^{-29} (300/T)^{2.8}$ $3.80 \times 10^{-11} (300/T)^{0.6}$	A
57	$CH_3O + NO_2 \xrightarrow{M} CH_3ONO_2$	(P) 0.6	$5.30 \times 10^{-29} (300/T)^{4.4}$ $1.90 \times 10^{-11} (300/T)^{1.8}$	A
58	$CH_3ONO_2 + OH \rightarrow HCHO + NO_2 + H_2O$		$5.00 \times 10^{-13} e^{810/T}$	A
59	$CH_3O_2 + HO_2 \rightarrow CH_3OOH + O_2$		$4.10 \times 10^{-13} e^{750/T}$	A
60	$CH_3O_2 + NO \rightarrow CH_3O + NO_2$		$2.80 \times 10^{-12} e^{300/T}$	A
61	$CH_3O_2 + NO_2 \xrightarrow{M} CH_3O_2NO_2$	(P) 0.6	$1.00 \times 10^{-30} (300/T)^{4.8}$ $7.20 \times 10^{-12} (300/T)^{2.1}$	A
62	$CH_3O_2NO_2 \xrightarrow{M} CH_3O_2 + NO_2$		$k_{61} / (1.30 \times 10^{-28} \times e^{11200/T})$	A
63	$CH_3O_2 + CH_3O_2 \rightarrow 2\ CH_3O + O_2$		$5.90 \times 10^{-13} e^{-509/T}$	B
64	$CH_3O_2 + CH_3O_2 \rightarrow HCHO + CH_3OH$		$7.04 \times 10^{-14} e^{365/T}$	B
65	$CH_3O_2 + CH_3C(O)OO \rightarrow CH_3O_2 + CH_3O + CO_2$		$2.00 \times 10^{-12} e^{500/T}$	A
66	$CH_3O_2 + CH_3C(O)OO \rightarrow CH_3COOH + HCHO + O_2$		$2.20 \times 10^{-13} e^{500/T}$	B
67	$CH_3COOH + OH \rightarrow CH_3O_2 + CO_2 + H_2O$		$4.00 \times 10^{-13} e^{200/T}$	A
68	$CH_3OOH + OH \rightarrow CH_3O_2 + H_2O$		$3.80 \times 10^{-12} e^{200/T}$	A
69	$C_2H_6 + OH \rightarrow C_2H_5O_2 + H_2O$		$8.70 \times 10^{-12} e^{-1070/T}$	A
70	$C_2H_5O_2 + NO \rightarrow C_2H_5O + NO_2$		$2.60 \times 10^{-12} e^{365/T}$	A
71	$C_2H_5O_2 + NO_2 \xrightarrow{M} C_2H_5O_2NO$	(P) 0.6	$1.20 \times 10^{-29} (300/T)^{4.0}$ 9.00×10^{-12}	A
72	$C_2H_5O_2NO_2 \xrightarrow{M} C_2H_5O_2 + NO_2$	(P) 0.31	$4.80 \times 10^{-4} e^{-9285/T}$ $8.80 \times 10^{15} e^{-10440/T}$	B
73	$C_2H_5O_2 + HO_2 \rightarrow ROOH + O_2$		$7.50 \times 10^{-13} e^{700/T}$	A
74	$C_2H_5O + O_2 \rightarrow CH_3CHO + HO_2$		$6.30 \times 10^{-14} e^{-550/T}$	A
75	$C_2H_5O + NO \xrightarrow{M} C_2H_5ONO$	(P) 0.6	$2.80 \times 10^{-27} (300/T)^{4.0}$ $5.00 \times 10^{-12} (300/T)^{1.0}$	A
76	$C_2H_5O + NO \rightarrow CH_3CHO + HO_2 + NO$		1.30×10^{-11}	B
77	$C_2H_5O + NO_2 \xrightarrow{M} C_2H_5ONO_2$	(P) 0.6	$2.00 \times 10^{-27} (300/T)^{4.0}$ $2.80 \times 10^{-11} (300/T)^{1.0}$	A
78	$C_3H_8 + OH \rightarrow C_3H_7O_2 + H_2O$		$1.00 \times 10^{-11} e^{-660/T}$	A
79	$C_3H_7O_2 + NO \rightarrow C_3H_7O + NO_2$		$2.70 \times 10^{-12} e^{-660/T}$	B
80	$C_3H_7O + O_2 \rightarrow CH_3COCH_3 + HO_2$		$1.40 \times 10^{-14} e^{-210/T}$	B
81	$C_3H_7O + NO \rightarrow C_3H_7ONO$		3.40×10^{-11}	B
82	$C_3H_7O + NO \rightarrow CH_3COCH_3 + HO_2 + NO$		6.50×10^{-12}	B
83	$C_3H_7O + NO_2 \rightarrow C_3H_7ONO_2$		3.50×10^{-11}	A

84	$C_2H_4 + OH \xrightarrow{M} HOC_2H_4O_2$	(P) 0.6	$1.00\times10^{-28}\,(300/T)^{0.8}$ 8.80×10^{-12}	A
85	$HOC_2H_4O_2 + NO \rightarrow NO_2 + 2\,HCHO + H$		6.93×10^{-12}	A
86	$HOC_2H_4O_2 + NO \rightarrow NO_2 + CH_3CHO + OH$		2.07×10^{-12}	A
87	$C_2H_4 + O_3 \rightarrow HCHO + H_2COO$		$4.48\times10^{-15}\,e^{-2630/T}$	A
88	$C_2H_4 + O_3 \rightarrow HCHO + HCOOH^*$		$7.52\times10^{-15}\,e^{-2630/T}$	A
89	$H_2COO + NO \rightarrow NO_2 + HCHO$		7.00×10^{-12}	C
90	$H_2COO + H_2O \rightarrow HCOOH + H_2O$		4.00×10^{-16}	C
91	$H_2COO + HCHO \rightarrow OZD$		2.00×10^{-12}	C
92	$H_2COO + CH_3CHO \rightarrow OZD$		2.00×10^{-12}	C
93	$H_2COO + ALD2 \rightarrow OZD$		2.00×10^{-12}	C
94	$HCOOH + OH \rightarrow H + CO_2 + H_2O$		4.00×10^{-13}	A
95	$HCOOH^* \rightarrow CO_2 + H_2$		0.21	C
96	$HCOOH^* \rightarrow CO + H_2O$		0.60	C
97	$HCOOH^* \rightarrow OH + HO_2 + CO$		0.19	C
98	$C_3H_6 + OH \xrightarrow{M} HOC_3H_6O_2$	(P) 0.5	$8.00\times10^{-27}\,(300/T)^{3.5}$ 3.00×10^{-11}	B
99	$HOC_3H_6O_2 + NO \rightarrow NO_2 + CH_3CHO + HCHO + HO_2$		6.00×10^{-12}	C
100	$C_3H_6 + O_3 \rightarrow HCHO + CH_3HCOO$		$4.88\times10^{-16}\,e^{-1900/T}$	A
101	$C_3H_6 + O_3 \rightarrow HCHO + CH_3HCOO^*$		$2.76\times10^{-15}\,e^{-1900/T}$	A
102	$C_3H_6 + O_3 \rightarrow CH_3CHO + H_2COO$		$1.22\times10^{-15}\,e^{-1900/T}$	A
103	$C_3H_6 + O_3 \rightarrow CH_3CHO + H_2COO^*$		$2.03\times10^{-15}\,e^{-1900/T}$	A
104	$CH_3HCOO + NO \rightarrow NO_2 + CH_3CHO$		7.00×10^{-12}	C
105	$CH_3HCOO + H_2O \rightarrow CH_3COOH + H_2O$		4.00×10^{-16}	C
106	$CH_3HCOO + HCHO \rightarrow OZD$		2.00×10^{-12}	C
107	$CH_3HCOO + CH_3CHO \rightarrow OZD$		2.00×10^{-12}	C
108	$CH_3HCOO + ALD2 \rightarrow OZD$		2.00×10^{-12}	C
109	$CH_3COOH^* \rightarrow CH_4 + CO_2$		0.16	C
110	$CH_3COOH^* \rightarrow CH_3O_2 + CO + OH$		0.64	C
111	$CH_3COOH^* \rightarrow CH_3O + CO + HO_2$		0.20	C
120	$HCHO + OH \rightarrow HO_2 + CO + H_2O$		$9.00\times10^{-12}\,e^{20/T}$	A
113	$HCHO + O \rightarrow OH + HO_2 + CO$		$3.40\times10^{-11}\,e^{-1600/T}$	A
114	$HCHO + NO_3 \rightarrow HNO_3 + HO_2 + CO$		5.80×10^{-16}	A
115	$HCHO + HO_2 \rightarrow HOCH_2O_2$		$6.70\times10^{-15}e^{605/T}$	A
116	$HOCH_2O_2 \rightarrow HO_2 + HCHO$		$2.40\times10^{12}\,e^{-7000/T}$	B
117	$HOCH_2O_2 + HO_2 \rightarrow ROOH$		$5.60\times10^{-15}\,e^{2300/T}$	B
118	$HOCH_2O_2 + NO \rightarrow NO_2 + HO_2 + HCOOH$		7.00×10^{-12}	C
119	$CH_3CHO + O \rightarrow CH_3C(O)OO + OH$		$1.80\times10^{-11}\,e^{-1100/T}$	A
120	$CH_3CHO + OH \rightarrow CH_3C(O)OO + H_2O$		$5.60\times10^{-12}\,e^{270/T}$	A
121	$CH_3CHO + NO_3 \rightarrow CH_3C(O)OO + HNO_3$		$1.40\times10^{-12}\,e^{-1900/T}$	A
122	$ALD2 + O \rightarrow CH_3C(O)OO + OH$		$1.80\times10^{-11}\,e^{-1100/T}$	A
123	$ALD2 + OH \rightarrow CH_3C(O)OO + H_2O$		$5.60\times10^{-12}\,e^{270/T}$	A
124	$ALD2 + NO_3 \rightarrow CH_3C(O)OO + HNO_3$		$1.40\times10^{-12}\,e^{-1900/T}$	A
125	$CH_3C(O)OO + HO_2 \rightarrow ROOH + O_2$		$4.30\times10^{-13}\,e^{1040/T}$	A
126	$CH_3C(O)OO + HO_2 \rightarrow CH_3O_2 + OH + CO_2$		$3.16\times10^{-13}\,e^{1040/T}$	C
127	$CH_3C(O)OO + NO \rightarrow NO_2 + CH_3O_2 + CO_2$		$8.10\times10^{-11}\,e^{270/T}$	A
128	$CH_3C(O)OO + NO_2 \xrightarrow{M} CH_3C(O)OONO_2$	(P) 0.6	$9.70\times10^{-29}\,(300/T)^{5.6}$	A

		$9.30\times10^{-12}\ (300/T)^{1.5}$	
129	$CH_3C(O)OONO_2 \xrightarrow{M} CH_3C(O)OO + NO_2$	k_{123} / $(9.0\times10^{-29} \times e^{14000/T})$	A
130	$CH_3C(O)OO + CH_3C(O)OO \rightarrow 2\ CH_3O_2 + O_2$	$2.90\times10^{-12}\ e^{500/T}$	A
131	$CH_3COCH_3 + OH \rightarrow CH_3COCH_2OO + H_2O$	$1.33\times10^{-13} + 3.82\times10^{-11}\ e^{-2000/T}$	A
132	$CH_3COCH_2OO + NO \rightarrow CH_3C(O)OO + HCHO + NO_2$	8.10×10^{-12}	C
133	$CH_3OH + OH \rightarrow HCHO + HO_2 + H_2O$	$6.21\times10^{-12}\ e^{-620/T}$	A
134	$CH_3OH + OH \rightarrow CH_3O + H_2O$	$1.09\times10^{-12}\ e^{-620/T}$	A
135	$C_2H_5OH + OH \rightarrow CH_3CHO + HO_2 + H_2O$	$6.52\times10^{-12}\ e^{-230/T}$	A
136	$C_2H_5OH + OH \rightarrow HOC_2H_4O_2 + H_2O$	$3.80\times10^{-13}\ e^{-230/T}$	A
137	$PAR + OH \rightarrow RO_2 + H_2O$	9.20×10^{-14}	C
138	$PAR + OH \rightarrow RO_2R + H_2O$	7.20×10^{-13}	C
139	$RO_2 + NO \rightarrow NO_2 + HO_2 + CH_3CHO + XOP$	7.70×10^{-12}	C
140	$RO_2 + NO \rightarrow NTR$	$4.40\times10^{-11}\ e^{-1400/T}$	C
141	$RO_2R + NO \rightarrow NO_2 + ROR$	7.00×10^{-12}	C
142	$RO_2R + NO \rightarrow NTR$	$1.20\times10^{-10}\ e^{-1400/T}$	C
143	$ROR + NO_2 \rightarrow NTR$	1.50×10^{-11}	C
144	$NTR \xrightarrow{M} RO_2 + NO_2$	k_{72}	B
145	$ROR \rightarrow KET + HO_2$	1.60×10^{3}	C
146	$ROR \rightarrow KET + DOP$	$2.10\times10^{14}\ e^{-8000/T}$	C
147	$ROR \rightarrow CH_3CHO + DOP + XOP$	$4.00\times10^{14}\ e^{-8000/T}$	C
148	$ROR \rightarrow CH_3COCH_3 + DOP + 2\ XOP$	$4.40\times10^{14}\ e^{-8000/T}$	C
149	$XOP + PAR \rightarrow$	6.80×10^{-12}	C
150	$DOP + PAR \rightarrow RO_2$	5.10×10^{-12}	C
151	$DOP + PAR \rightarrow AO_2 + 2\ XOP$	1.50×10^{-12}	C
152	$DOP + PAR \rightarrow RO_2R$	1.70×10^{-13}	C
153	$DOP + KET \rightarrow CH_3C(O)OO + XOP$	6.80×10^{-12}	C
154	$AO_2 + NO \rightarrow NO_2 + CH_3COCH_3 + HO_2$	8.10×10^{-12}	C
155	$OLE + O \rightarrow 2\ PAR$	$4.10\times10^{-12}\ e^{-324/T}$	C
156	$OLE + O \rightarrow CH_3CHO$	$4.10\times10^{-12}\ e^{-324/T}$	C
157	$OLE + O \rightarrow HO_2 + CO + RO_2$	$1.20\times10^{-12}\ e^{-324/T}$	C
158	$OLE + O \rightarrow RO_2 + XOP + CO + HCHO + OH$	$2.40\times10^{-12}\ e^{-324/T}$	C
159	$OLE + OH \rightarrow CH_3O_2 + CH_3CHO + XOP$	$5.20\times10^{-12}\ e^{504/T}$	C
160	$OLE + O_3 \rightarrow CH_3CHO + H_2COO + XOP$	$2.80\times10^{-15}\ e^{-2105/T}$	C
161	$OLE + O_3 \rightarrow HCHO + CH_3HCOO + XOP$	$2.80\times10^{-15}\ e^{-2105/T}$	C
162	$OLE + O_3 \rightarrow CH_3CHO + HCOOH^* + XOP$	$4.30\times10^{-15}\ e^{-2105/T}$	C
163	$OLE + O_3 \rightarrow HCHO + CH_3COOH^* + XOP$	$4.30\times10^{-15}\ e^{-2105/T}$	C
164	$OLE + NO_3 \rightarrow PNO_2$	7.70×10^{-15}	C
165	$PNO_2 + NO \rightarrow DNIT$	6.80×10^{-13}	C
166	$PNO_2 + NO \rightarrow HCHO + CH_3CHO + XOP + 2NO_2$	6.80×10^{-12}	C
167	$C_4H_6 + OH \rightarrow CH_3O_2 + CH_3CHO$	$1.48\times10^{-11}\ e^{448/T}$	D
168	$C_4H_6 + O_3 \rightarrow 0.5\ CH_3CHO + 0.197\ H_2COO + XOP + 0.5\ HCHO + 0.197\ CH_3HCOO + 0.303\ H_2COO^* + 0.303\ CH_3HCOO^* + OLE$	$2.20\times10^{-14}\ e^{-2431/T}$	E
169	$C_4H_6 + NO_3 \rightarrow PNO_2 + C_2H_4$	1.03×10^{-13}	D
Aromatic Chemistry			

170	$C_6H_6 + OH \rightarrow 0.4\ BO_2 + 0.4\ H_2O + 0.6\ CRES + 0.6\ HO_2 + XOP$	$3.10\times10^{-12}\ e^{-270/T}$	D
171	$TOL + OH \rightarrow BO_2 + H_2O$	$1.70\times10^{-13}\ e^{322/T}$	C
172	$TOL + OH \rightarrow CRES + HO_2$	$7.60\times10^{-13}\ e^{322/T}$	C
173	$TOL + OH \rightarrow TO_2$	$1.20\times10^{-12}\ e^{322/T}$	C
174	$BO_2 + NO \rightarrow NO_2 + BZA + HO_2$	8.10×10^{-12}	C
175	$BZA + OH \rightarrow BZO_2 + H_2O$	1.30×10^{-11}	C
176	$BZO_2 + NO \rightarrow NO_2 + PHO_2 + CO_2$	2.50×10^{-12}	C
177	$BZO_2 + NO_2 \rightarrow PBZN$	8.40×10^{-12}	E
178	$PBZN \rightarrow BZO_2 + NO_2$	$1.60\times10^{15}\ e^{-13033/T}$	E
179	$PHO_2 + NO \rightarrow NO_2 + PHO$	8.10×10^{-12}	C
180	$PHO + NO_2 \rightarrow NPHN$	$1.30\times10^{-11}\ e^{300/T}$	E
181	$CRES + OH \rightarrow CRO + H_2O$	1.60×10^{-11}	C
182	$CRES + OH \rightarrow CRO_2 + H_2O$	2.50×10^{-11}	C
183	$CRES + NO_3 \rightarrow CRO + HNO_3$	2.20×10^{-11}	C
184	$CRO + NO_2 \rightarrow NCRE$	1.40×10^{-11}	C
185	$CRO_2 + NO \rightarrow NO_2 + OPEN + HO_2$	4.00×10^{-12}	C
186	$CRO_2 + NO \rightarrow NO_2 + ACID + HO_2$	4.00×10^{-12}	C
187	$TO_2 + NO \rightarrow NO_2 + OPEN + HO_2$	7.30×10^{-12}	C
188	$TO_2 + NO \rightarrow NTR$	8.10×10^{-13}	C
189	$TO_2 \rightarrow HO_2 + CRES$	4.20	C
190	$XYL + OH \rightarrow CRES + PAR + HO_2$	$3.32\times10^{-12}\ e^{116/T}$	C
191	$XYL + OH \rightarrow XLO_2 + H_2O$	$1.70\times10^{-12}\ e^{116/T}$	C
192	$XYL + OH \rightarrow TO_2$	$5.00\times10^{-12}\ e^{116/T}$	C
193	$XYL + OH \rightarrow XINT$	$6.60\times10^{-12}\ e^{116/T}$	C
194	$XLO_2 + NO \rightarrow NO_2 + HO_2 + BZA + PAR$	8.10×10^{-12}	C
195	$XINT + NO \rightarrow NO_2 + HO_2 + 2\ CH_3COCHO + PAR$	8.10×10^{-12}	C
196	$CH_3COCHO + OH \rightarrow MGPX + H_2O$	1.50×10^{-11}	B
197	$MGPX + NO \rightarrow NO_2 + CH_3C(O)OO + CO_2$	8.10×10^{-12}	C
198	$OPEN + OH \rightarrow OPPX + CH_3C(O)OO + HO_2 + CO$	3.00×10^{-11}	C
199	$OPEN + O_3 \rightarrow CH_3CHO + MGPX + HCHO + CO$	$1.60\times10^{-18}\ e^{-500/T}$	C
200	$OPEN + O_3 \rightarrow HCHO + CO + OH + 2\ HO_2$	$4.30\times10^{-18}\ e^{-500/T}$	C
201	$OPEN + O_3 \rightarrow CH_3COCHO$	$1.10\times10^{-17}\ e^{-500/T}$	C
202	$OPEN + O_3 \rightarrow CH_3C(O)OO + HCHO + HO_2 + CO$	$3.20\times10^{-17}\ e^{-500/T}$	C
203	$OPEN + O_3 \rightarrow$	$5.40\times10^{-18}\ e^{-500/T}$	C
204	$OPPX + NO \rightarrow NO_2 + HCHO + HO_2 + CO$	8.10×10^{-12}	C
	Terpene Chemistry		
200	$ISOP + OH \rightarrow ISOH$	$2.55\times10^{-11}\ e^{410,2/T}$	F,G
201	$ISOP + O_3 \rightarrow 0.17\ MACR + 0.378\ MVK + 0.664\ OH + 0.054\ PAR + 0.054\ OLE + 0.054\ H_2COO + 0.5\ HCHO + 0.366\ HO_2 + 0.068\ CO_2 + 0.461\ CO + 0.366 RO2R + 0.121\ ACID$	$7.86\times10^{-15}\ e^{-1912.9/T}$	G,H
202	$ISOP + O \rightarrow 0.22\ MACR + 0.63\ MVK + 0.08\ ISOH$	3.50×10^{-11}	F,G
203	$ISOP + NO_3 \rightarrow ISNT$	$3.02\times10^{-12}\ e^{-445.9/T}$	F,G
204	$ISOH + NO \rightarrow 0.364\ MACR + 0.477\ MVK + 0.840\ HCHO + 0.08\ ISNI1 + 0.08\ ISNI2 + 0.886\ HO_2 + 0.840\ NO_2$	$1.22\times10^{-11}\ e^{-180/T}$	F
205	$ISNT + NO \rightarrow 1.1\ NO_2 + 0.8\ HO_2 + 0.80\ ISNI1 + 0.1\ MACR + 0.15\ HCHO + 0.05\ MVK + 0.05\ DISN$	$1.39\times10^{-11}\ e^{-180/T}$	F

206	ISNI1 + OH $\rightarrow$ ISNIR	3.35×10^{-11}	F
207	ISNI2 + OH $\rightarrow$ ISNIR	1.88×10^{-11}	F
208	ISNIR + NO $\rightarrow$ 0.05 DISN + 0.05 HO_2 + 1.9 NO_2 + 0.95 CH_3CHO + 0.95 CH_3COCH_3	$1.39\times10^{-11}\ e^{-180/T}$	F
209	ISNI1 + O_3 $\rightarrow$ 0.2 O + 0.08 OH + 0.5 HCHO + 0.5 IALD1 + 0.5 ISNI2 + 0.5 NO_2	5.00×10^{-18}	F
210	ISOH + ISOH $\rightarrow$ 0.6 MACR + 0.6 MVK + 1.2 HCHO + 1.2 HO_2	2.00×10^{-13}	F
211	ISOH + HO_2 $\rightarrow$ IPRX	$6.15\times10^{-11}\ e^{-900/T}$	F
212	IPRX + OH $\rightarrow$ ISOH	2.00×10^{-11}	F
213	IPRX + O_3 $\rightarrow$ 0.7 HCHO	8.00×10^{-18}	F
214	MACR + O_3 $\rightarrow$ 0.8 CH_3COCHO + 0.7 HCHO + 0.2 O + 0.09 H_2COO + 0.2 CO + 0.275 HO_2 + 0.215 OH + 0.16 CO_2 + 0.15 CH_2CCH_3CHOO	$1.36\times10^{-15}\ e^{-2113.7/T}$	F,H
215	MVK + O_3 - $\rightarrow$ 0.5 CH_3COCHO + 0.5 HCHO + 0.2 H_2O + 0.2 CO_2 + 0.56 CO + 0.28 HO_2 + 0.36 OH + 0.1 CH_3CHO + 0.28 CH_3CO_3 + 0.12 ACID + 0.12 UNR	$7.50\times10^{-16}\ e^{-1519.9/T}$	H
216	MACR + OH $\rightarrow$ 0.42 MAC1 + 0.08 MAC2 + 0.5 $CH_2CCH_3C(O)OO$	$1.86\times10^{-11}\ e^{175/T}$	F
217	MVK + OH $\rightarrow$ 0.28 MV1 + 0.72 MV2	$4.11\times10^{-12}\ e^{453/T}$	F
218	MAC1 + NO $\rightarrow$ 0.95 HO_2 + 0.95 CO + 0.95 CH_3COCH_3 + 0.95 NO_2 + 0.05 ISNI2	$1.39\times10^{-11}\ e^{-180/T}$	F
219	MAC2 + NO $\rightarrow$ 0.95 HO_2 + 0.95 HCHO + 0.95 CH_3COCHO + 0.95 NO_2 + 0.05 ISNI2	$1.39\times10^{-11}\ e^{-180/T}$	F
220	MV1 + NO $\rightarrow$ 0.95 CH_3COCHO + 0.95 HCHO + 0.05 ISNI2 + 0.95 NO_2 + 0.95 HO_2	$1.39\times10^{-11}\ e^{-180/T}$	F
221	MV2 + NO $\rightarrow$ 0.95 CH_3CHO + 0.95 $CH_3C(O)OO$ + 0.05 ISNI2 + 0.95 NO_2	$1.39\times10^{-11}\ e^{-180/T}$	F
222	MV1 + HO_2 $\rightarrow$ ROOH	$6.15\times10^{-11}\ e^{-900/T}$	F
223	MV2 + HO_2 $\rightarrow$ ROOH	$6.15\times10^{-11}\ e^{-900/T}$	F
224	MAC1 + HO_2 $\rightarrow$ ROOH	$6.15\times10^{-11}\ e^{-900/T}$	F
225	MAC2 + HO_2 $\rightarrow$ ROOH	$6.15\times10^{-11}\ e^{-900/T}$	F
226	$CH_2CCH_3C(O)OO$ + NO_2 $\rightarrow$ MPAN	8.40×10^{-12}	F
227	MPAN $\rightarrow$ $CH_2CCH_3C(O)OO$ + NO_2	$1.58\times10^{16}\ e^{-13507/T}$	F
228	$CH_2CCH_3C(O)OO$ + NO $\rightarrow$ C_2H_4 + CH_3O_2 + NO_2 + CO_2	1.40×10^{-11}	F
229	TERPH + OH $\rightarrow$ RO227	1.77×10^{-10}	H
230	TERPH + O_3 $\rightarrow$ 0.445 CO + 0.055 H_2O_2 + 0.89 OH + 0.11 UNR + 0.445 RO229 + 0.445 RO230	1.40×10^{-16}	H
231	TERPH + O $\rightarrow$ UNR	8.59×10^{-11}	H
232	TERPH + NO_3 $\rightarrow$ RO228	2.91×10^{-11}	H
233	RO227 + NO $\rightarrow$ 0.38 AP8 + 0.62 NO_2 + 0.62 HO_2 + 0.62 UNR	$8.89\times10^{-13}\ e^{180.2/T}$	H
234	RO227+ RO2R $\rightarrow$ HO_2 + UNR + RO2R + O_2	1.00×10^{-15}	H
235	RO227 + HO_2 $\rightarrow$ OH + HO_2 + UNR	$3.41\times10^{-13}\ e^{800.2/T}$	H
236	RO228 + NO $\rightarrow$ 2 NO_2 + UNR	$8.89\times10^{-13}\ e^{180.2/T}$	H
237	RO228 + RO2R $\rightarrow$ NO_2 + RO2R + O_2 + UNR	1.00×10^{-15}	H
238	RO229 + HO_2 $\rightarrow$ OH + HO_2 + UNR	$3.41\times10^{-13}\ e^{800.2/T}$	H
239	RO229 + NO $\rightarrow$ 0.23 AP9 + 0.77 NO_2 + 0.77 RO240	$1.05\times10^{-12}\ e^{180.2/T}$	H

240	RO229 + RO2R $\rightarrow$ RO240 + RO2R + O_2	1.00×10^{-15}	H
241	RO230 + NO $\rightarrow$ NO_2 + CH_3CO_3 + UNR	$8.89\times10^{-13}\ e^{180.2/T}$	H
242	RO230 + RO2R $\rightarrow$ CH_3CO_3 + RO2R + O_2 + UNR	1.00×10^{-15}	H
243	RO230 + HO_2 $\rightarrow$ OH + CH_3CO_3 + UNR	$3.41\times10^{-13}\ e^{800.2/T}$	H
244	RO240 + NO $\rightarrow$ NO_2 + CH_3CO_3 + ALD2 + PAR	$1.05\times10^{-12}\ e^{180.2/T}$	H
245	RO240 + RO2R $\rightarrow$ CH_3CO_3 + ALD2 + PAR + RO2R + O_2	1.00×10^{-15}	H
246	RO240 + HO_2 $\rightarrow$ OH + CH_3CO_3 + ALD2 + PAR	$3.41\times10^{-13}\ e^{800.2/T}$	H
247	AP8 + OH $\rightarrow$ NO_2 + H_2O + UNR	1.03×10^{-10}	H
248	AP9 + OH $\rightarrow$ NO_2 + H_2O + UNR	9.07×10^{-11}	H
	Sulfur Chemistry		
249	SO_2 + OH $\xrightarrow{M}$ HSO_3 (P) 0.6	$3.00\times10^{-31}\ (300/T)^{3.3}$ 1.50×10^{-12}	A
250	SO_2 + O + M $\rightarrow$ SO_3 + M	$1.30\times10^{-33}\ (300/T)^{-3.6}$	A
251	HSO_3 + O_2 $\rightarrow$ SO_3 + HO_2	$1.30\times10^{-12}\ e^{-330/T}$	A
252	SO_3 + H_2O + H_2O $\rightarrow$ H_2SO_4 + H_2O	$8.50\times10^{-41}\ e^{6540/T}$	A
253	CH_3SCH_3 + OH $\rightarrow$ $CH_3SCH_2O_2$ + H_2O	$1.10\times10^{-11}\ e^{-240/T}$	A
254	CH_3SCH_3 + OH $\rightarrow$ $CH_3S(OH)CH_3$	f	A
255	$CH_3SCH_2O_2$ + NO $\rightarrow$ CH_3SCH_2O + NO_2	8.00×10^{-12}	I
256	CH_3SCH_2O $\rightarrow$ CH_3S + HCHO	1.00×10^{1}	I
257	CH_3S + O_2 $\rightarrow$$CH_3SOO$*	3.00×10^{-18}	A
258	CH_3SOO* + NO $\rightarrow$ CH_3SO + NO_2	1.4×10^{-11}	I
259	CH_3SOO* $\rightarrow$ CH_3S + O_2	6.0×10^{2}	I
260	CH_3SO + O_3 $\rightarrow$ CH_3SO_2 + O_2	6.0×10^{-13}	A
261	CH_3SO_2 $\rightarrow$ CH_3O_2 + SO_2	1.1×10^{1}	I
262	$CH_3S(OH)CH_3$ $\rightarrow$ CH_3SOH + CH_3O_2	5.0×10^{5}	I
263	CH_3SOH + OH $\rightarrow$ CH_3SO + H_2O	1.1×10^{-10}	I
	Photoprocesses		
264	O_2 + hν $\rightarrow$ O + O		A
265	O_3 + hν $\rightarrow$ O(^1D) + O_2		A
266	O_3 + hν $\rightarrow$ O + O_2		A
267	HO_2 + hν $\rightarrow$ OH + O(^1D)		A
268	H_2O + hν $\rightarrow$ H + OH		A
269	H_2O_2 + hν $\rightarrow$ 2 OH		A
270	NO_2 + hν $\rightarrow$ NO + O		A
271	NO_3 + hν $\rightarrow$ NO_2 + O		B
272	NO_3 + hν $\rightarrow$ NO + O_2		B
273	N_2O + hν $\rightarrow$ N_2 + O(1D)		A
274	N_2O_5 + hν $\rightarrow$ NO_2 + NO_3		A
275	HONO + hν $\rightarrow$ OH + NO		A
276	HONO + hν $\rightarrow$ H + NO_2		A
277	HNO_3 + hν $\rightarrow$ OH + NO_2		A
278	HNO_3 + hν $\rightarrow$ HONO + O(^1D)		A
279	HNO_3 + hν $\rightarrow$ OH + NO + O		A
280	HO_2NO_2 + hν $\rightarrow$ HO_2 + NO_2		B
281	HO_2NO_2 + hν $\rightarrow$ OH + NO_3		B
282	HCHO + hν $\rightarrow$ 2 HO_2 + CO		A
283	HCHO + hν $\rightarrow$ CO + H_2		A
284	CH_3OOH + hν $\rightarrow$ CH_3O + OH		B
285	CH_3CHO + hν $\rightarrow$ CH_3O_2 + HO_2 + CO		B
286	ALD2 + hν $\rightarrow$ CH_3O_2 + HO_2 + CO		B

287	$CH_3ONO + h\nu \rightarrow CH_3O + NO$		C
288	$CH_3ONO_2 + h\nu \rightarrow CH_3O + NO_2$		B
289	$CH_3O_2NO_2 + h\nu \rightarrow CH_3O_2 + NO_2$		B
290	$C_2H_5ONO_2 + h\nu \rightarrow C_2H_5O + NO_2$		B
291	$C_3H_7ONO_2 + h\nu \rightarrow C_3H_7O + NO_2$		B
292	$CH_3CO_3NO_2 + h\nu \rightarrow CH_3CO_3 + NO_2$		A
293	$CH_3COCH_3 + h\nu \rightarrow CH_3O_2 + CH_3C(O)OO$		B
294	$KET + h\nu \rightarrow CH_3C(O)OO + RO_2 + 2XOP$		J
295	$MVK + h\nu \rightarrow CH_3C(O)OO + C_2H_4 + HO_2$		K
296	$MACR + h\nu \rightarrow C_2H_4 + HO_2 + CO + CH_3O_2$		A
297	$CH_3COCHO + h\nu \rightarrow CH_3C(O)OO+CO+HO_2$		B
298	$BZA + h\nu \rightarrow PHO_2 + CO + HO_2$		C
299	$OPEN + h\nu \rightarrow CH_3C(O)OO + CO + HO_2$		C

Species names are defined in Appendix Table B.3. of Jacobson (*S17*). In addition, C_4H_6=1,3-butadiene, C_6H_6=benzene., ALD2=C_3 and higher aldehydes, TERPH = monoterpenes. Species above reaction arrows are second or third bodies included in pressure-dependent reactions (footnote *a*) or in thermal dissociation reactions in equilibrium with the forward (previous) reaction. M is total air. The "Ref." column refers to sources of data for reaction rate coefficients, absorption cross sections, and quantum yields.

a (P) indicates a pressure-dependent reaction, for which the reaction rate coefficient is

$$k_r = \frac{k_{\infty,T} k_{0,T}[\mathrm{M}]}{k_{\infty,T} + k_{0,T}[\mathrm{M}]} F_c^{\left[1+\left(\log_{10}\frac{k_{0,T}[\mathrm{M}]}{k_{\infty,T}}\right)^2\right]^{-1}}$$

where $k_{0,T}$ is the temperature-dependent three-body, low-pressure limit rate coefficient (the first rate listed), $k_{\infty,T}$ is the two-body, high-pressure limit rate coefficient (the second rate listed), [M] = [N_2] + [O_2] is the concentration (molecules cm^{-3}) of the third body, and F_c is the broadening factor.

b A, JPL Evaluation (*S18*); B, Atkinson et al. (*S19*); C, Gery et al. (*S20*); D, MCM Mechanism (*S21*); E, Bahta et al. (*S22*) (assume products the same as OLE+O_3 plus OLE; F, Paulson and Seinfeld (*S23*); G, Atkinson (*S24*); H, Griffin et al. (*S25*); G, Yin et al. (*S26*); H, assumed the same as for acetone; I, assumed the same as for methyl ethyl ketone.

c $k_r = k_1 + k_3[\mathrm{M}] / (1 + k_3[\mathrm{M}]/k_2)$, where $k_1 = 2.40\times10^{-14}\ e^{460/T}$, $k_2 = 2.70\times10^{-17}\ e^{2199/T}$, $k_3 = 6.50\times10^{-34}\ e^{1335/T}$, and [M] = [$N_2$] + [$O_2$] (molecules cm^{-3}).

d $k_r = 1.50\times10^{-13}(1+0.6\ p_a)(300/T)^{1.0}$, where p_a is the ambient air pressure in atmospheres.

e $k_r = (2.30\times10^{-13}\ e^{600/T} + 1.70\times10^{-33}[\mathrm{M}]e^{1000/T})(1. + 1.40\times10^{-21}[H_2O]e^{2200/T})$, where [M] = [$N_2$] + [$O_2$] and [$H_2O$] are in units of molecules cm^{-3}.

f $k_r = 1.0\times10^{-39}[\mathrm{M}]e^{5820/T}/(1+5.0\times10^{-30}[\mathrm{M}]e^{6280/T})$, where [M] = [$N_2$] + [$O_2$] (molecules cm^{-3}) .

1.C. Aerosol Processes

For the present application, aerosol processes were treated in a single size distribution consisting of 17 size bins ranging from 0.002 to 50 μm in diameter, and multiple aerosol components per bin (black carbon, primary organic matter, secondary organic matter, H_2O, H^+, NH_4^+, Na^+, H_2SO_4, HSO_4^-, SO_4^{2-}, NO_3^-, Cl^-, NH_4NO_3, $(NH_4)_2SO_4$, C_2H_5OH, CH_5CHO, HCHO, C_4H_6, C_6H_6, soildust, pollen, spores, bacteria. The model is generalized though, so that any number of discrete, interacting aerosol size distributions can be used for aerosol processes (*S27*) and cloud development (*S28*). The aerosol size bin structure used was the moving-center structure, whereby bin edges were fixed but bin centers moved in diameter space due to change in particle size (*S2*). Parameters treated prognostically in each size bin included particle number concentration and individual component mole concentration. Single-particle volume was calculated assuming particles

contained a solution and nonsolution component, as in (*S27*), which also describes most numerical techniques used for solving aerosol physical and chemical processes.

Size-dependent aerosol processes included emission, homogeneous nucleation, condensation, dissolution, aerosol-aerosol coagulation, aerosol-cloud/ice/graupel coagulation, equilibrium hydration of liquid water, internal-particle chemical equilibrium, irreversible aqueous chemistry, evaporation of cloud drops to aerosol-particles, transport, sedimentation, dry deposition, rainout, and washout. Aerosol particles affected solar and thermal-IR radiation, cloud evolution, gas concentration, and surface albedo, all of which fed back to meteorology.

Sulfuric acid-water binary homogeneous nucleation rates were calculated as in (*S29*); sulfuric acid-ammonia-water ternary homogeneous nucleation rates were calculated as in (*S30*). Homogeneous nucleation and condensation of sulfuric acid were solved simultaneously between the gas phase and all size bins with a mass-conserving, noniterative, and unconditionally stable scheme (*S27*) that also solved condensation of condensable secondary organic matter onto size-resolved aerosol particles. The model further treated nonequilibrium dissolutional growth of inorganics (e.g., NH_3, HNO_3, HCl) and several organics (C_2H_5OH, CH_5CHO, HCHO, C_4H_6, C_6H_6) to all size bins with a mass-conserving nonequilibrium growth solver, PNG-EQUISOLV II (*S31*), where PNG is Predictor of Nonequilibrium Growth. EQUISOLV II is a chemical equilibrium solver that determines aerosol liquid water content, pH, and ion distributions following nonequilibrium growth (*S32*). Aerosol-aerosol coagulation was solved among all size bins and components and among total particles in each bin with a volume-conserving, noniterative, algorithm (*S27*). Coagulation kernels included those for Brownian motion, Brownian diffusion enhancement, van der Waals forces, viscous forces, fractal geometry of soot aggregates, turbulent shear, turbulent inertial motion, and gravitational settling.

1.D. Gas-Aerosol-Cloud-Turbulence Interactions

On the regional scale, cloud thermodynamics and microphysics were calculated explicitly and clouds were transported in three dimensions. Water vapor and size- and composition-resolved aerosol particles were first transported using predicted horizontal and vertical velocities. When the partial pressure of water vapor exceeded the saturation vapor pressure over liquid water or ice on an aerosol particle or pre-existing hydrometeor-particle surface, water vapor condensed or deposited. The saturation vapor pressure and the critical radius for aerosol activation were affected by the Kelvin effect and Raoult's law, both of which were calculated from aerosol and hydrometeor composition. Thus, changes in, for example, surface tension due to organics and inorganics affected the activation properties of aerosol particles. The numerical solution for hydrometeor growth accounted for water vapor condensation and deposition onto all activated size-resolved aerosol particles and pre-existing size-resolved hydrometeor simultaneously, as in (*S12*). The numerical scheme was unconditionally stable, noniterative, positive-definite, and mole conserving.

During the condensation/deposition calculation, liquid drops and/or ice crystals grew from a single size-resolved aerosol distribution into separate liquid and/or ice hydrometeor size distributions, where each discrete size bin of the liquid and ice distributions contained all the chemical components of the underlying CCN aerosol particles. A third discretized hydrometeor distribution, graupel, was also tracked. This distribution formed upon heterocoagulation of the liquid water and ice hydrometeor distributions, contact freezing of aerosol particles with the liquid distribution, heterogeneous-homogeneous freezing of the liquid distribution, and evaporative freezing of the liquid distribution.

Following partitioning, the size-resolved cloud-aerosol processes treated each time step included hydrometeor-hydrometeor coagulation (liquid-liquid, liquid-ice, liquid-graupel, ice-ice, ice-graupel, and graupel-graupel), aerosol-hydrometeor coagulation, large liquid drop breakup, settling to the layer below (or precipitation from the lowest layer to the surface), evaporative cooling during drop settling, evaporative freezing (freezing during drop cooling), heterogeneous-homogeneous freezing, contact freezing, melting, evaporation, sublimation release of aerosol cores upon evaporation/sublimation, coagulation of hydrometeors with interstitial aerosols, irreversible aqueous chemistry, gas washout, and lightning generation from size-resolved coagulation among ice hydrometeors. The kernel for all cloud coagulation interactions and aerosol-cloud coagulation interactions included a coalescence efficiency and collision kernels for Brownian motion, Brownian diffusion enhancement, turbulent inertial motion, turbulent shear, settling, thermophoresis, diffusiophoresis, and electric charge. Numerical techniques used for these processes are given in (*S28*).

During the microphysical calculations, changes in energy due to condensation, evaporation, deposition, sublimation, freezing, and melting were included as diabatic heating terms in the thermodynamic energy equation; energy was conserved due to cloud formation and decay. Similarly, total water (water vapor, size-resolved aerosol water, size-resolved cloud water, soil water, and ocean water) was conserved.

Following the cloud- and aerosol microphysical calculations each time step, size-resolved aerosol particles and hydrometeors particles (if they existed) in each grid cell were transported by modeled horizontal and vertical winds and turbulence. Thus, three-dimensional size-resolved clouds (stratus, cumulus, cumulonimbus, cirrus, etc.) formed, moved, and dissipated in the model.

Aerosol particles of different size were removed by size-resolved clouds and precipitation through two mechanisms: nucleation scavenging and aerosol-hydrometeor coagulation. Both processes were size-resolved with respect to both aerosol particles and hydrometeor particles.

On the global scale, cloud thermodynamics was calculated with stratus and cumulus parameterizations whereas cloud microphysics was calculated explicitly, as described in (*S28*). The stratus cloud scheme was from (*S33*) and was coupled with the calculation of turbulence (order 2.5). The stratus scheme predicted cloud fraction and cloud water content in each layer given turbulence terms and vertical gradients in potential temperature and moisture. Turbulence parameters affected clouds, momentum, energy, and tracers, particularly in the boundary layer, which was resolved. Cumulus clouds were predicted with a modified Arakawa-Schubert algorithm (*S34*). In each column, nearly 500 subgrid cumulus clouds could form (and 1-10 typically formed), each defined by a unique cloud base and top (when 23 layers existed below the tropopause, 22 bases and 22 tops are possible). For each subgrid cloud, water and energy transport were solved with a mass-flux convection scheme; gas and size-resolved aerosol component transport were solved with a positive-definite, stable convective plume transport scheme. For each subgrid cloud, the model also generated adjustments to large-scale potential temperature, momentum, and water vapor.

Following cumulus-parameterization convection on the global scale, the bulk water predicted in each layer from the cumulus and stratus parameterizations were evaporated/sublimated, then regrown (simultaneously for liquid and ice) onto the size-resolved aerosol distributions transported vertically to that layer. Because aerosol particles were transported vertically with cloud water in all cases, aerosol activation was consistent with that in a rising plume. The remainder of the microphysical calculation,

including all interaction of aerosol particles with clouds, was the same as on the regional scale. The main difference between the global and regional calculations was that, on the global scale, all remaining cloud water was evaporated at the end of a time step and clouds were allowed to reform during the next step; on the regional scale, clouds that formed were tracked continuously and allowed to evolve over time. In both cases, the first and second indirect effects were treated. In other words, aerosol particles affected cloud drop size and optical properties and precipitation rates.

In sum, on the global scale, cumulus and stratus parameterizations were used to determine subgrid clouds and cloud water, and cloud microphysics was calculated as a time-dependent process following an equilibrium calculation of cloud thermodynamics. Clouds were not transported but were developed locally. On the regional scale, however, clouds evolved and developed during time-dependent explicit thermodynamics and microphysics and were transported in three dimensions.

1.E. Radiative Processes

Radiation processes included UV, visible, solar-IR, and thermal-IR interactions with gases, size/composition-resolved aerosols, and size/composition-resolved hydrometeor particles. Radiative transfer was solved with the scheme of (*S35*). Calculations were performed for >600 wavelengths/probability intervals and affected photolysis and heating. Gas absorption coefficients in the solar-IR and thermal-IR were calculated for H_2O, CO_2, CH_4, CO, O_3, O_2, N_2O, CH_3Cl, $CFCl_3$, CF_2Cl_2, and CCl_4, from HITRAN data (*S36*). Aerosol-particle optical properties were calculated assuming that black carbon (BC) (if present in a size bin) comprised a particle's core and all other material coated the core. Shell real and imaginary refractive indices for a given particle size and wavelength were obtained by calculating the solution-phase refractive index, calculating refractive indices of non-solution, non-BC species, and volume averaging solution and nonsolution refractive indices. Core and shell refractive indices were used in a core-shell Mie-theory calculation (*S37*). Cloud liquid, ice, and graupel optical properties for each hydrometeor size and radiation wavelength were also determined from Mie calculations that accounted for absorbing inclusions. For such a calculation, nonspherical ice crystals were assumed to be a collection of spheres of the same total volume to area ratio and total volume (*S38*). The surface albedos of snow, sea ice, and water (ocean and lake) were wavelength-dependent and predicted by (rather than specified in) the model (*S10*). Column calculations treated shading by structures (e.g., buildings) and topography.

1.F. Subgrid Surfaces and Oceans

The model treated ground temperatures over subgrid surfaces (up to 12 soil classes and roads over soil, roofs over air, and water in each cell). It also treated vegetation over soil, snow over bare soil, snow over vegetation over soil, sea-ice over water, and snow over sea-ice over water (*S6*). For all surfaces except sea ice and water, surface and subsurface temperatures and liquid water were found with a time-dependent 10-layer module. Ocean mixed-layer velocities, energy transport, and mass transport were calculated with a gridded 2-D potential-enstrophy, energy, and mass-conserving shallow-water equation module, forced by wind stress (*S39*), based on a shallow-water scheme (*S13*). The actual depth at each location was a prognostic variable, but because the module conserved volume exactly, the average mixing depth over the global ocean was constant (80 m). For lake water, a fixed 80 m mixing depth was assumed. Water (ocean and lake) temperatures were also affected by sensible, latent, and radiative fluxes. Nine additional layers existed below each ocean mixed-layer grid cell to treat energy diffusion from the mixed layer to the deep ocean and ocean chemistry. Dissolution of gases to the ocean and ocean chemistry were calculated with OPD-EQUISOLV O (*S40*), where OPD solves nonequilibrium transport between the ocean and atmosphere and EQUISOLV O solves

chemical equilibrium in the ocean. Both schemes are mass conserving and unconditionally stable.

2. Description of Emissions and Simulations

The model was run in nested mode from the global to local scale for a future August in two domains, one focused on Los Angeles and the other, over the U.S. as a whole. Simulations were also run for a future February in the Los Angeles domain. Three one-way nested domains were used for Los Angeles simulations: a global domain (4°-SN x 5°-WE resolution), a California domain (0.2°x0.15° ≈ 21.5 km x 14.0 km with the southwest corner grid cell centered at 30.0 °N and -126.0° W and 60 SN cells x 75 WE cells), and a South Coast Air Basin (SCAB) domain (0.045 °x0.05 ° ≈ 4.7 km x 5 km with the southwest corner grid cell centered at 30.88 °N and –119.35° W and 46 SN cells x 70 WE cells). Two nested domains were used for the U.S. simulations: the global domain and a U.S. domain (0.5 °x0.75°). The global domain included 39 sigma-pressure layers between the surface and 0.425 hectaPascal (hPa). All nested regional domains included 26 layers between the surface and 103.5 hPa, matching the bottom 26 global-domain layers exactly. All domains included five layers in the bottom 1 km. The nesting time interval for passing meteorological and chemical variables was one hour in all cases. All physical processes described, including emissions, were solved in all nested domains, including the global domain, of all simulations.

The baseline emission inventory used was the U.S. National Emission Inventory (NEI) for 2002 (*S41*), modified for future gasoline and E85 vehicle fleets. The inventory accounts for over 370,000 stack and fugitive sources, 250,000 area sources, and 1700 source classification code (SCC) categories of onroad and nonroad mobile sources. The inventory provides emissions of nitrogen oxides (NO_x), carbon monoxide, ammonia, sulfur dioxide, total organic gas, and coarse and fine particulate matter either at a specific location (point sources) or in a county (all others). In the case of county emissions, these pollutants were distributed to each model grid cell in each model domain with high-resolution population, roadway, and building data (*S41*). The pollutants were then distributed temporally (at 1-hour resolution over the year) with temporal distribution factors for each source classification code (*S41*). Finally, the organic pollutants were distributed into explicit chemicals and into carbon bond groups with speciation profiles for each source classification code and chemical/bond group distributions for each speciation profile from (*S42*).

The 2002 fossil-fuel inventory was forecast to 2020 by reducing all mobile-source emissions (gasoline and nongasoline onroad and nonroad) by 60%, which is approximately consistent with two independent estimates. Streets (*S43*), for example, derived speciated 2030:2000 emission factors by sector and world region assuming IPCC SRES A1B and B1 emission scenarios. Table S2 shows results for the U.S. transportation sector. An across-the board reduction of 60% mobile emissions for 2020 assumed here is conservative because it is greater than the 2030 reductions in Table S2, interpolated to 2020, for most species. Second, Table S3 shows that the California Air Resources Board (CARB) estimates that total organic gas (TOG) emissions in the South Coast Air Basin (SCAB) may decrease 57.7% between 2002 and 2020, from 172,919 to 73,192 metric tonnes/yr. Although the 60% reduction assumed here is consistent with CARB, the CARB estimate may be optimistic since it exceeds the estimated 2020 reduction interpolated from Table S2; thus, the 60% reduction estimated here may be conservative.

Table S2. Derived (*S43*) percent emission changes by species between 2000 and 2030 in the U.S. transportation sector under the IPCC SRES A1B and B1 emission scenarios.

	Mobile	Mobile

	A1B	B1
Carbon monoxide	-45	-67
Nitrogen oxides as NO_2	-49	-67
Methane	+19	-8
Paraffin bond group	-44	-65
Ethene	-58	-70
Olefin bond group	-56	-70
Alcohols	-58	-70
Formaldehyde	+18	-44
Higher aldehydes	-57	-70
Ketones	0	0
Toluene bond group	-56	-69
Xylene bond group	-58	-70
Isoprene bond group	0	0
Unreactive organic gases	-7	-29
Sulfur oxides as SO_2	-65	-74
Ammonia	0	0
Particulate organic matter	-51	-61
Particulate black carbon	-51	-61
Particulate sulfate	-51	-61
Particulate nitrate	0	0
Total $PM_{2.5}$	-51	-61
Total PM_{10}	-51	-61

Table S3. Comparison of total organic gas (TOG) emissions (metric tonnes/yr) from the California Air Resources Board emission inventory with those from the U.S. NEI for 2002. Also shown are 2020 emission estimates used here for gasoline and E85 fleets.

	Onroad gasoline or E85	Onroad non-gasoline	Total onroad	Nonroad gasoline or E85	Nonroad non-gasoline	Total nonroad	Total mobile
2002 CARB SCAB[1]			122,178			50,741	172,919
2002 CARB model domain[2]			143,632			59,651	203,283
2002 NEI model domain[3]	167,272	5398	172,670	57,423	15,700	73,123	245,793
2020 CARB estimate SCAB[1]			41,210			31,982	73,192
2020 CARB model domain[2]			48,447			37,598	86,045
2020 NEI model domain[4]	66,914	2159	69,073	22,969	6280	29,249	98,322
2020 E85 model domain[5]	81,569	2159	83,728	27,895	6280	34,175	117,903

1) (*S44*)
2) The model domain is slightly larger than the SCAB. CARB emissions in the model domain were estimated by multiplying CARB emissions in the SCAB domain by 1.1756, the ratio of the populations of the model domain in 2000 (17,267,158) to that in the SCAB domain in 2000 (14,687,964) (Table 4 of the main text).
3) 2002 NEI emissions for the model domain were obtained from the U.S. NEI (*S41*).
4) 2020 NEI emissions with a gasoline fleet were estimated as 40% of 2002 NEI emissions.

The resulting 2020 inventory for Los Angeles is given in Table 1 of the main text. The resulting inventory for the U.S. as a whole is given in Table S4.

Table S4. Same as Table 1 of the main text, but for the U.S. model domain.

Species	(1) 2020	(2) 2020	(3) 2020	(4)	(5) Case 1	(6) 2020

	Baseline onroad gasoline (tonnes/yr)	Baseline nonroad gasoline (tonnes/yr)	Baseline total gasoline (tonnes/yr)	Percent change from gasoline to E85	E85 replacing 2020 total gasoline (tonnes/yr)	Baseline and E85 non-gasoline (tonnes/yr)
Carbon monoxide	2.22×10^{7}	6.84×10^{6}	2.90×10^{7}	+5	3.05×10^{7}	1.96×10^{7}
Nitrogen oxides as NO_2	1.55×10^{6}	75,100	1.62×10^{6}	-30	1.14×10^{6}	1.12×10^{7}
Organic gases						
Methane	175,000	85,600	261,000	+43	373,000	3.71×10^{6}
Ethane	24,800	12,100	37,000	0	37,000	346,000
Propane	9630	3700	14,300	-65	5020	186,500
Paraffin bond group	886,000	435,000	1.32×10^{6}	-80	264,200	4.75×10^{6}
Ethene	71,300	35,000	106,000	-17	88,200	430,000
Propene	19,500	9580	29,100	-65	10,200	76,300
1,3-Butadiene	28,900	14,100	43,000	-10	38,700	18,700
Olefin bond group	18,900	9290	28,200	-17	23,400	173,000
Methanol	0	0	0	0	0	27,800
Ethanol	0	0	0	*	2.06×10^{6}	306,000
Formaldehyde	13,200	6470	19,700	+60	31,500	90,300
Acetaldehyde	4820	2350	7170	+2000	143,000	21,800
Higher aldehydes	68,300	33,600	101,900	-60	40,700	258,000
Formic acid	0	0	0	0	0	5720
Acetic acid	0	0	0	0	0	11,600
Acetone	0	0	0	0	0	106,000
Benzene	25,300	12,400	37,800	-79	7940	144,000
Toluene bond group	127,000	62,100	189,000	-80	37,800	1.30×10^{6}
Xylene bond group	236,000	115,000	351,000	-80	70,300	1.79×10^{6}
Isoprene bond group	1290	631	1920	-80	383	5510
Unreactive	91,300	44,700	136,000	-80	27,200	1.24×10^{6}
Total organic gas	1.80×10^{6}	883,000	2.68×10^{6}	+22	3.26×10^{6}	1.50×10^{7}
Sulfur oxides as SO_2	63,100	2990	66,100	0	66,100	1.54×10^{7}
Ammonia	101,000	1870	103,000	0	103,000	4.26×10^{6}
$PM_{2.5}$						
Organic matter	10,400	18,700	29,100	0	29,100	1.60×10^{6}
Black carbon	3480	1910	5390	0	5390	291,000
Sulfate	593	107	700	0	700	146,000
Nitrate	25.6	150	176	0	176	15,500
Other	3810	3020	6830	0	6830	7.24×10^{6}
Total $PM_{2.5}$	18,300	23,900	42,200	0	42,200	9.29×10^{6}
PM_{10}						
Organic matter	18,600	21,500	40,100	0	40,100	3.88×10^{6}
Black carbon	6220	2200	8410	0	8410	513,000
Sulfate	1060	123	1180	0	1180	248,000
Nitrate	45.8	173	218	0	218	52,500
Other	6800	3470	10,300	0	10,300	3.42×10^{7}
Total PM_{10}	32,700	27,500	60,200	0	60,200	3.89×10^{7}

*Please see footnote to Table 1 of the main text.

The model also treated natural emissions not treated in the NEI and both natural and anthropogenic emissions outside of the U.S. (up to the global scale). Biogenic emissions were derived by combining 1-km vegetation and land-use data for the U.S. (*S45*, BELD3) and 1-km landuse/landcover data for the rest of the world (*S46*) with emission factors for each landuse type to determine normalized (at a specific temperature

and radiation level) inventories of biogenic isoprene, monoterpenes, other VOCs, and NO emission for any spatial and temporal grid. Normalized data were combined in the model with temperature- and radiation-dependent correction factors (*S47*) to derive emission rates affected by the current temperatures and radiation fields. As shown in Table S1, isoprene (ISOP) and monoterpenes (TERPH) were treated as distinct species.

On the global scale, baseline black carbon (BC) and primary organic carbon (POC) emissions from most fossil fuels and biofuels at 1^{o}x1^{o} resolution were from (*S48*). Shipping BC and POC emissions were obtained by scaling BC emission factors to the sulfur shipping emission rate (*S49*), as described in (*S50*). Aircraft emissions were derived by applying BC, POC, and sulfate emission factors to the 1999 commercial, military, and charter aircraft fuel use data of (*S51*, *S52*). Monthly biomass-burning BC and POC emissions were from (*S53*). Emission rates of particle components K^+, Na^+, Ca^{2+}, Mg^{2+}, NH_4^+, Cl^-, SO_4^{2-}, and NO_3^-, and gases CO_2, CO, CH_4, H_2, H_2O, N_2O, NO_x, SO_2, ethene, propene, ethane, and propane from biomass burning and from biofuel burning were obtained by multiplying the gridded BC biofuel or biomass emission rates by the ratio of the mean biofuel or biomass emission factor for each gas or particle component to that of BC (*S54*).

Additional emission types treated in the model were wind-driven soil dust, sea spray, pollen, and spores, NO_x from lightning, DMS from the oceans, volcanic SO_2, and CO_2, H_2, and H_2O from fossil-fuel combustion and biomass burning. Molecular hydrogen emissions, for example, were proportional to carbon monoxide emissions from fossil-fuel vehicles (*S11*). Emitted sea spray and spume-drop components include H_2O, POC, K^+, Na^+, Ca^{2+}, Mg^{2+}, Cl^-, SO_4^{2-}. Sea-spray emissions versus size were calculated by combining the parameterizations of (*S55, S56*). The composition of emitted sea spray was that of sea water. Ocean-atmosphere exchange of DMS and all other gases was calculated as described in (*S40*). Sea water DMS concentrations were estimated from (*S57*). Soil dust emissions versus size, soil type, and wind speed were calculated from (*S58*) using soil data from (*S59*). Sporadic and continuous volcanic SO_X emissions were from (*S60*). NO_x from lightning was calculated from size-resolved interactions among in-cloud hydrometeors, as described in (*S17*). Additional global-scale monthly NO_x CO, and speciated organic gas emissions were from (*S61*). Additional NH_3 were from (*S62*). Additional CH_4 were from (*S63*), scaled to the present. Additional CO_2 were from (*S64*).

Baseline and sensitivity simulations were run for a future August in both the global-through-Los Angeles and global-through-U.S. domains and for a future February in the Los Angeles domain. For each sensitivity simulation, only the finest-resolved domain was perturbed (e.g., by changing emissions) to minimize any impacts of perturbations to the coarse-resolution domains that might feed into the finest-resolved domains.

The model dynamics time steps were 300 s (global domain), 10 s (California and U.S. domains), and 5 s (Los Angeles domain). The time interval for nesting between the domains was 1 hour. Variables passed at the horizontal boundaries included temperature, specific humidity, wind velocity, gas concentrations (including total water as water vapor), and size- and composition-resolved aerosol concentrations. Clouds themselves were treated with no-flux boundary conditions since total water as water vapor moved across boundaries and could generate new clouds; however, there is no reason why clouds could not be passed across the boundaries as well for future studies.

Although future-year emissions were used, initial meteorological conditions were obtained from National Center for Environmental Prediction (NCEP) reanalysis fields for August 1, 1999, at 12 GMT (*S65*). U.S., surface meteorological data from over 1650

stations (*S66*) were assimilated with the NCEP data at the time corresponding to initialization for each domain. Similarly, aerosol and gas fields in all domains were initialized from background data. U.S. EPA ambient air quality data (*S66*) for O_3, CO, NO_2, SO_2, $PM_{2.5}$, and PM_{10} were then assimilated with background values at the initial time. No data assimilation, nudging, or model spinup was performed during any simulation.

3. Discussion of Results

Future simulations with vehicles using gasoline and E85 were performed for the Los Angeles and U.S. cases.

3.A. Mixing Ratio Changes in Los Angeles

Figure S1 shows August-averaged near-surface mixing ratios or concentrations from the Case 1 E85 simulation (corresponding to 2020 E85 emissions from Table 1 of the main text) and the difference between the Case 1 E85 simulation and the gasoline simulation, for the Los Angeles model domain. Figure S5 shows the same for the U.S. domain.

In terms of emitted species, E85 increased unburned ethanol in the most populated area of Los Angeles by up to about 20 ppbv (Fig. S1.a), acetaldehyde by up to 1.5 ppbv (Fig. S1.b), formaldehyde by up to 0.2 ppbv (Fig. S1.c), methane by up to 5 ppbv (Fig. S1.d), carbon monoxide by up to 30 ppbv (Fig. S1.e), and molecular hydrogen by up to 13 ppbv (Fig. S1.f). E85 decreased nitrogen dioxide by up to 5 ppbv (Fig. S1.g), 1,3-butadiene by up to 0.05 ppbv (Fig. S1.h), benzene by up to 0.2 ppbv (Fig. S1.i), toluene by up to 0.9 ppbv (Fig. S1.j), and xylene by up to 1.2 ppbv (Fig. S1.k).

S1.a.

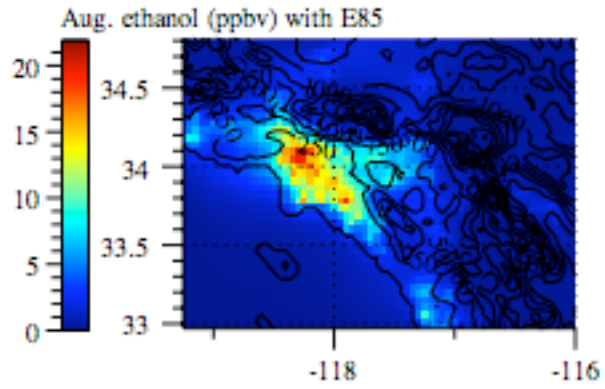

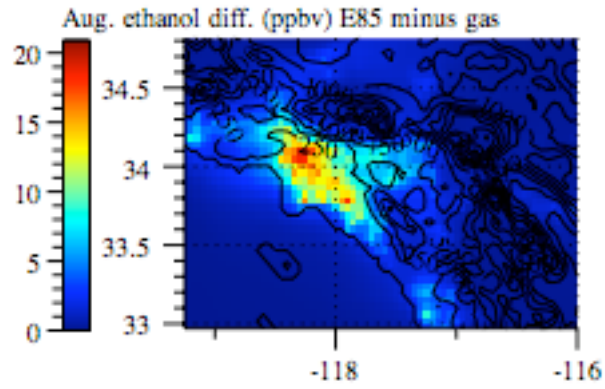

S1.b.

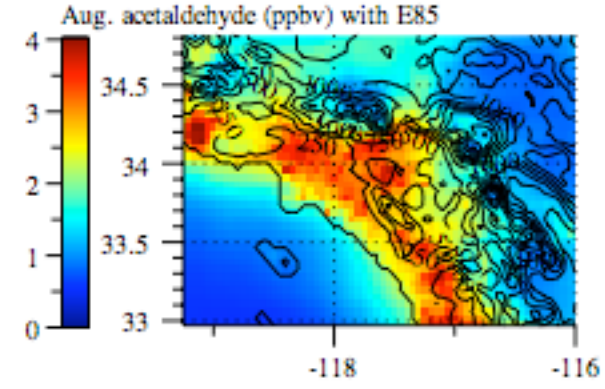

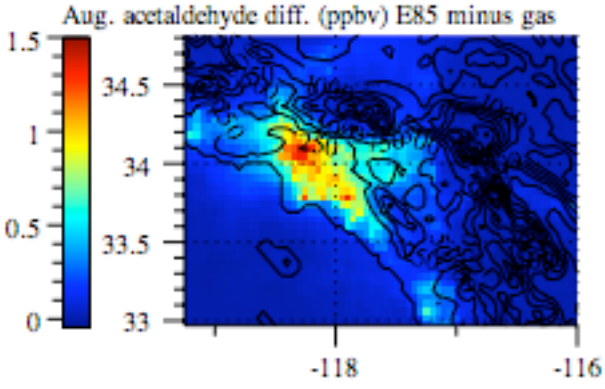

S1.c.

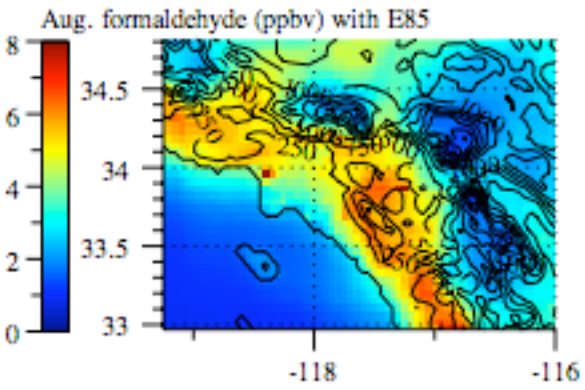

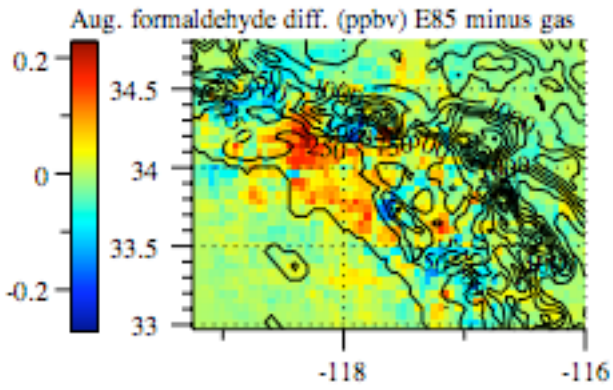

S1.d.

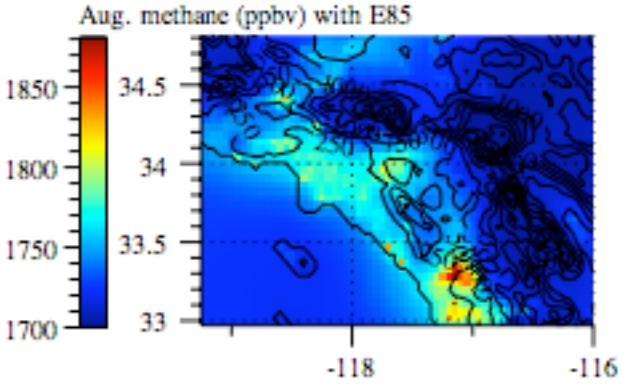

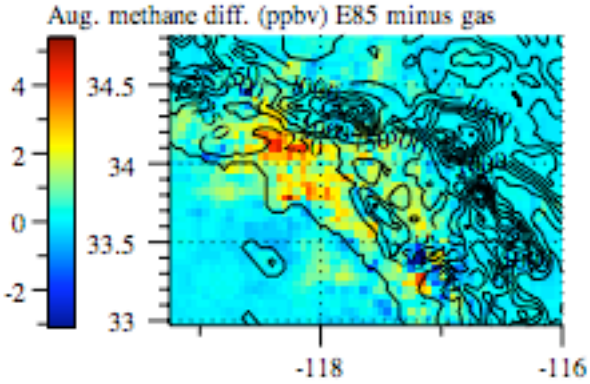

S1.e.

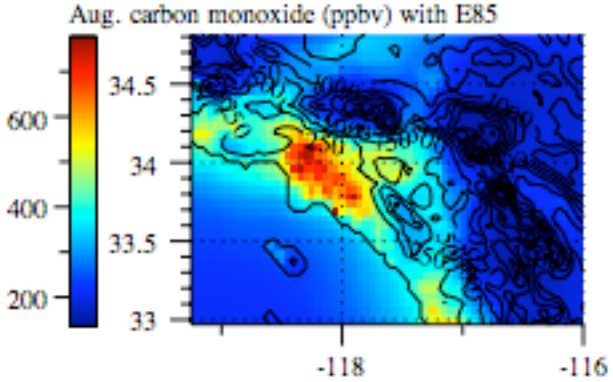

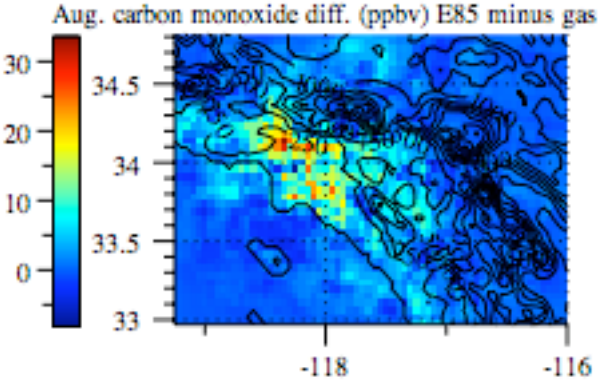

S1.f.

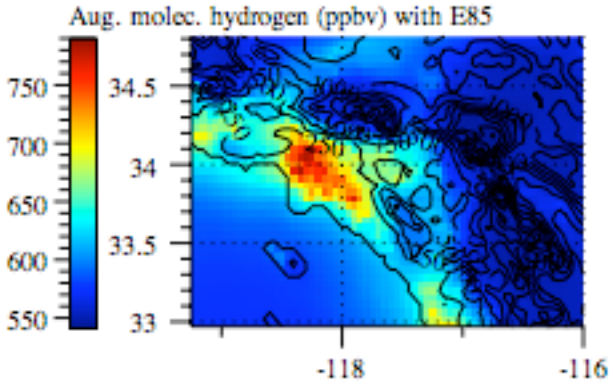

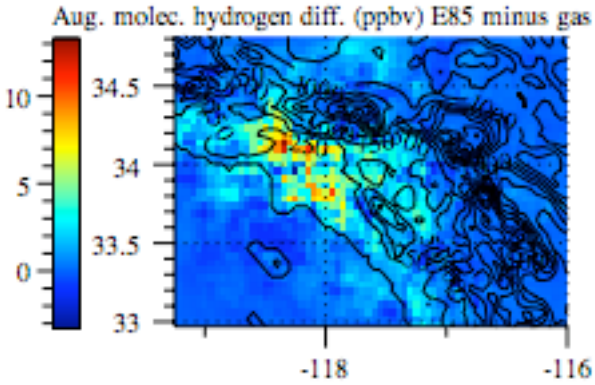

S1.g.

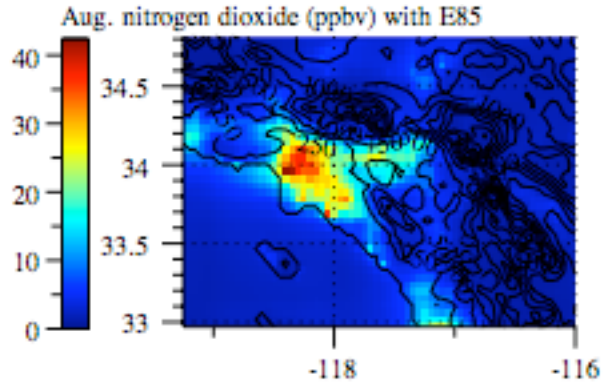

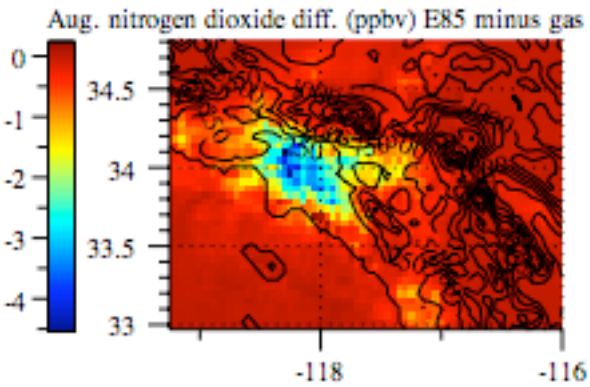

S1.h.

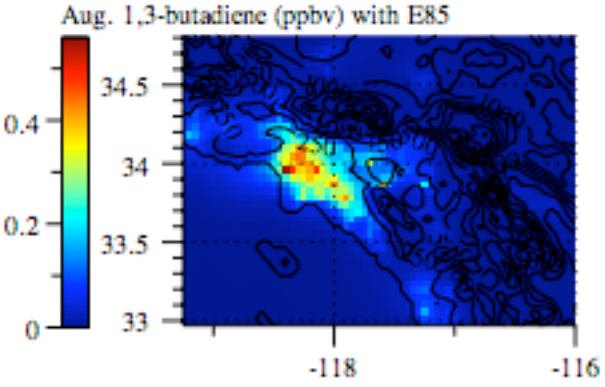

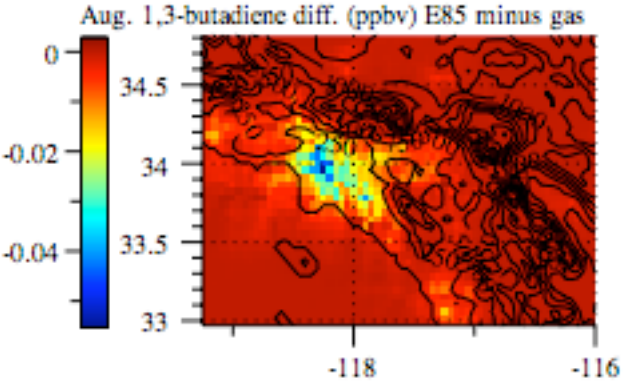

S1.i.

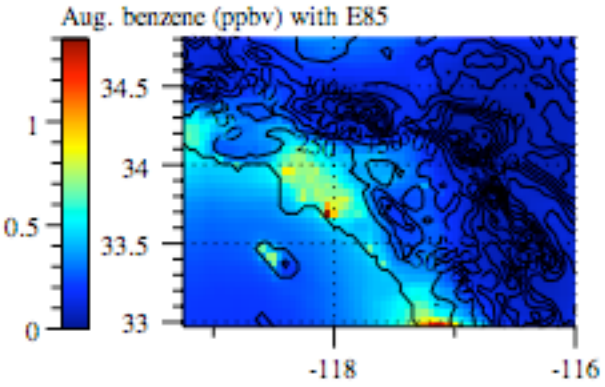

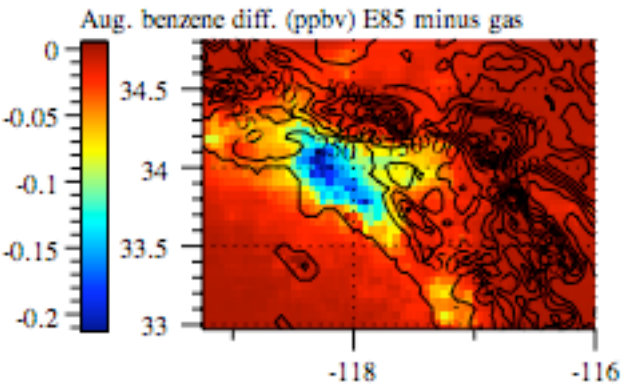

S1.j.

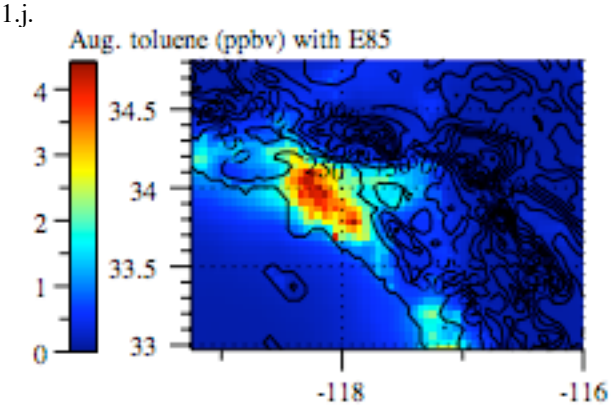

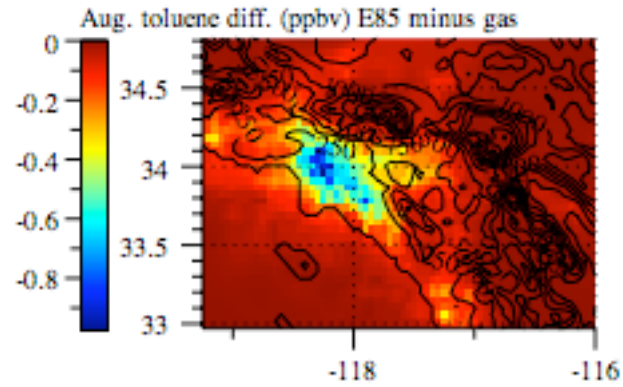

S1.k.

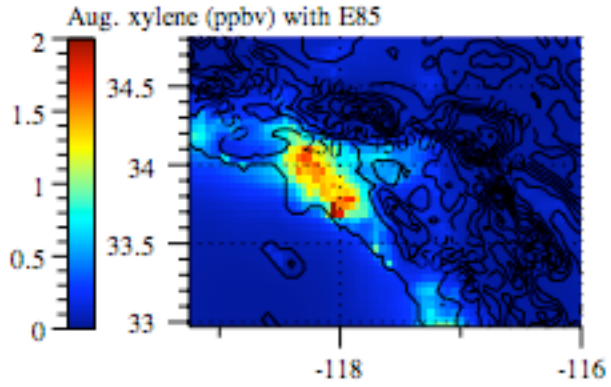

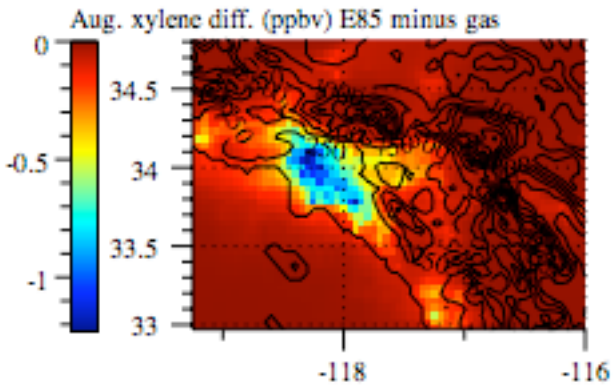

S1.l.

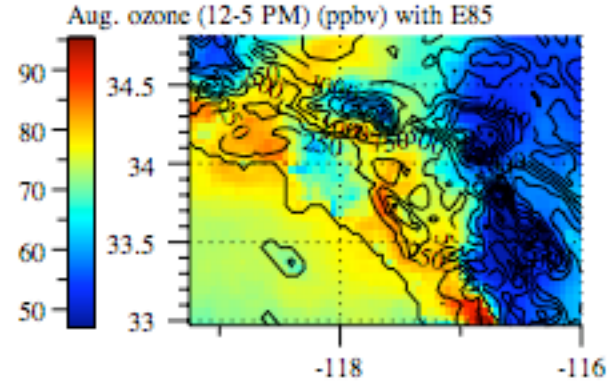

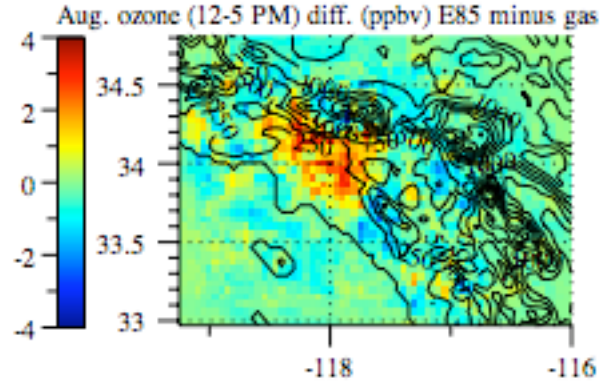

S1.m.

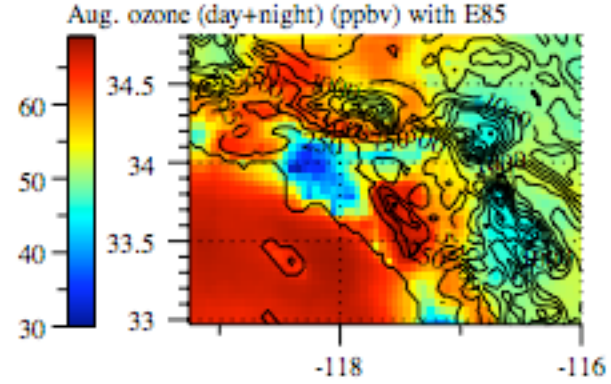

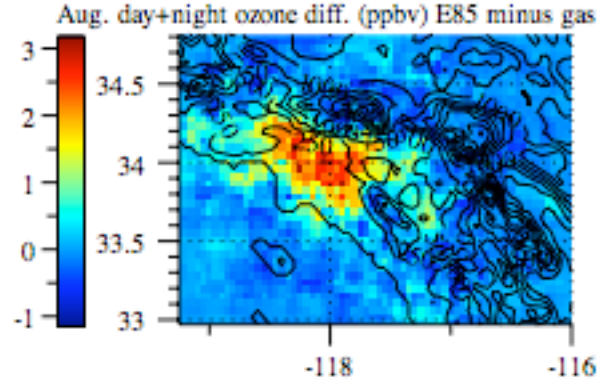

S1.n.

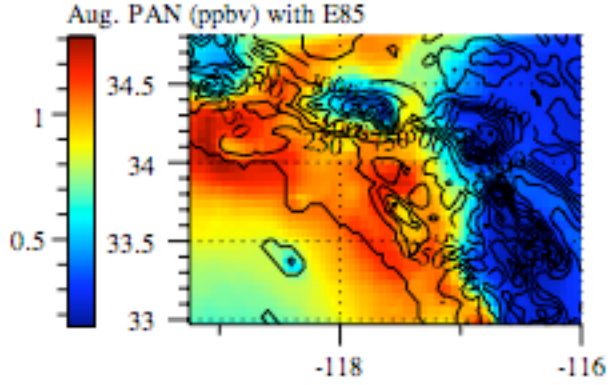

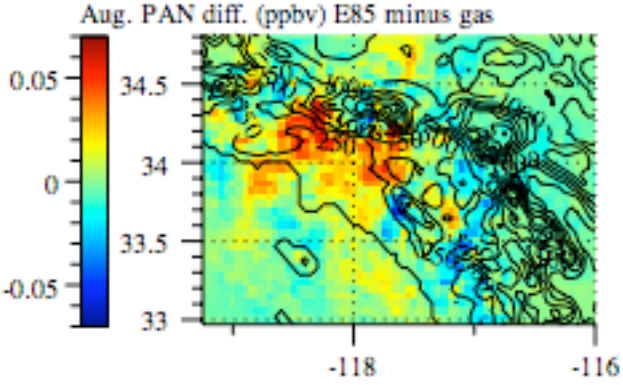

S1.o.

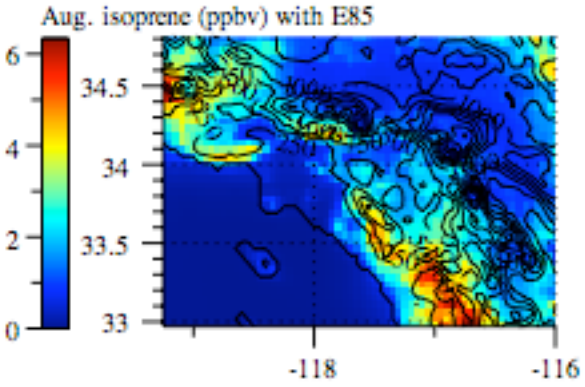

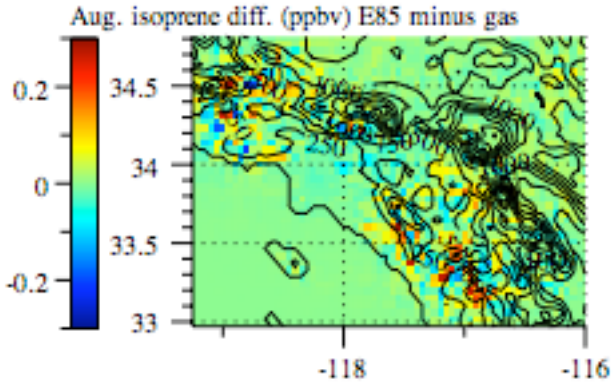

S1.p.

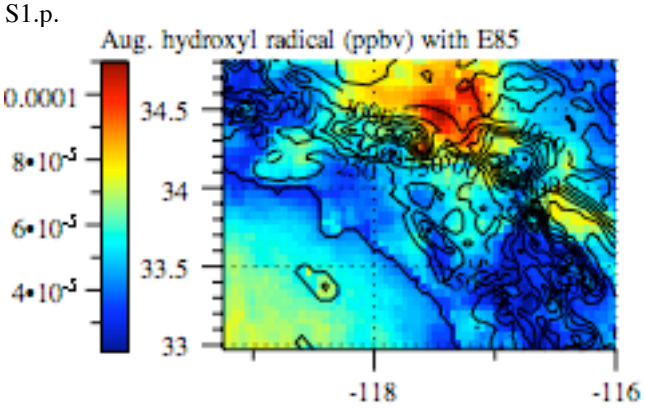

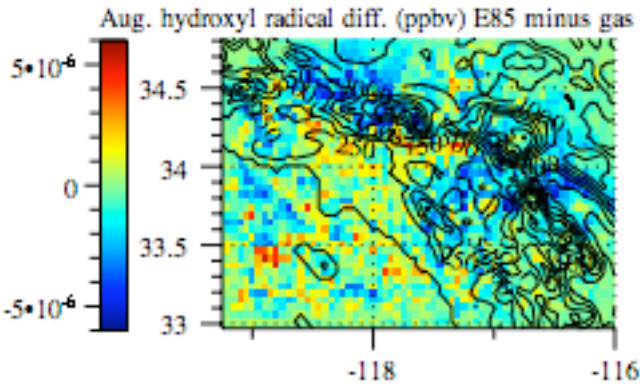

S1.q.

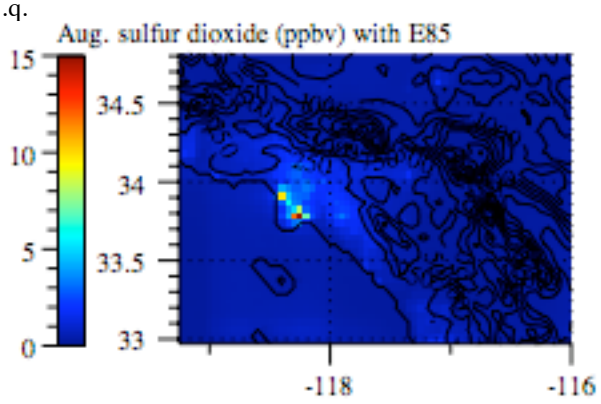

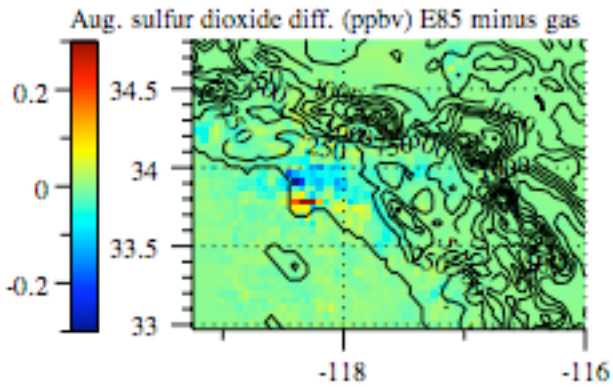

S1.r.

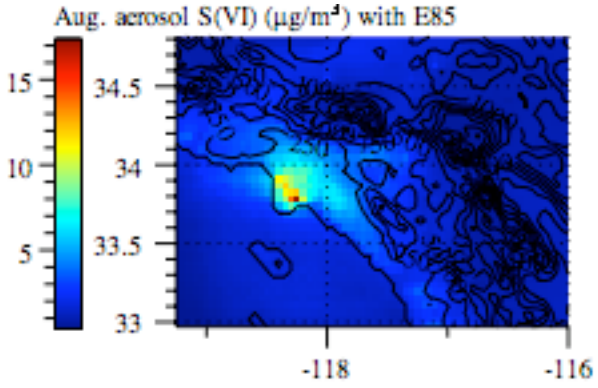

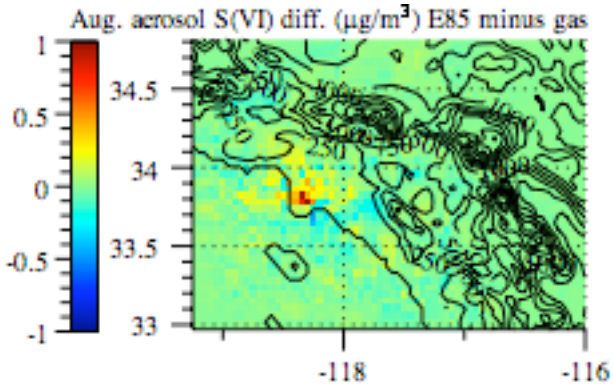

S1.s.

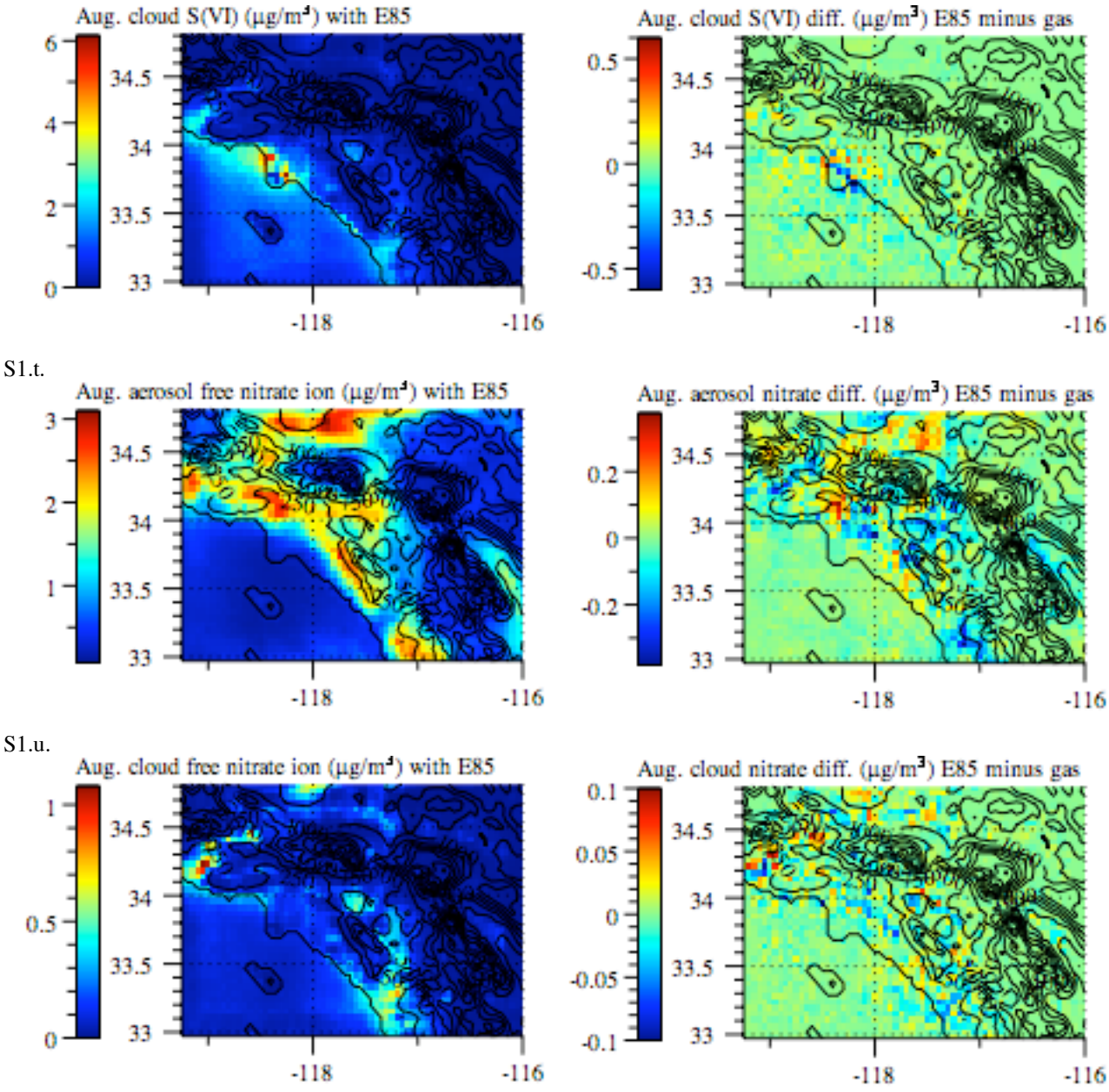

Figure S1. August monthly averaged near-surface modeled mixing ratios or concentrations in the Los Angeles domain from the Case 1 E85 simulation (left column) and from the difference between the Case 1 E85 simulation and the gasoline simulation (right column). All plots give 24-hour-, monthly-averaged values except for Fig. S1.l, which gives 12-5 PM-, monthly-averaged values.

Figs. S1.l and S1.m show that E85 increased peak daytime (12-5 PM) ozone by up to 4 ppbv and day plus night average ozone by up to 3 ppbv, respectively. The increases occurred in populated areas, as seen by comparing these plots with the population distribution shown in Fig. 2 of the main text. Some ozone decreases occurred in less populated areas surrounding the main part of the basin. The increase in ozone due to E85 can be explained in terms of an ozone isopleth (Fig. S2). Los Angeles is in the upper triangle of the isopleth, where the ambient ratio ROG:NO_x<8:1. Table 1 of the main text, for example, shows that the emission ratio, ROG:NO_x < 8:1 in Los Angeles. In

this region of the isopleth, either a decrease in nitrogen oxides (NO_x) or an increase in reactive organic gases (ROGs) increases ozone. E85 both decreases NO_x and increases ROGs; thus, E85 should theoretically increase ozone relative to gasoline in the Los Angeles basin. This result was confirmed by the model.

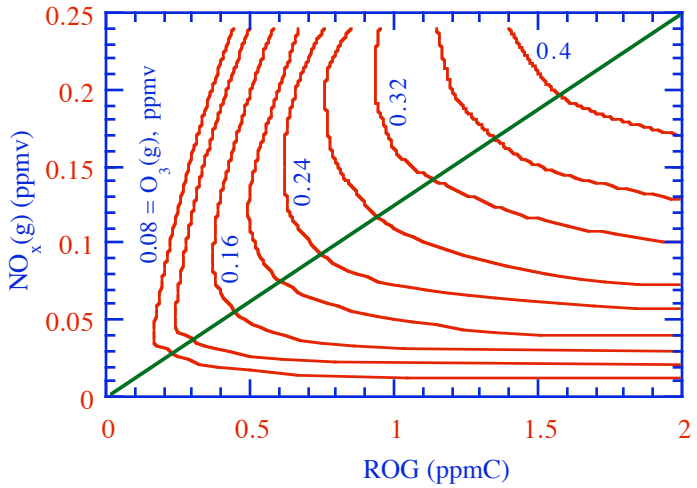

Figure S2. Example of an ozone isopleth (*S67*), which shows peak ozone mixing ratios resulting from different initial mixing ratios of oxides of nitrogen (NO_x) and reactive organic gases (ROG). The ROG:NO_x ratio along the line through zero is 8:1.

Four sensitivity simulations under 2020 emission conditions were run for the Los Angeles model domain in August. When E85 NO_x emissions were reduced by 45% rather than 30% relative to gasoline (Case 2, Fig. S3.a), E85 increased ozone further relative to Case 1. The reason was that, since Los Angeles is high in the upper triangle of the ozone isopleth (Fig. S2), significant reductions in NO_x increase ozone more than lesser reductions. When E85 NO_x emissions were reduced by 15% rather than 30% relative to gasoline (Case 3, Fig. S3.b), E85 increased ozone relative to gasoline, but less than in Case 1. When E85 total organic gas (TOG) emissions were increased by 6% rather than 22% relative to gasoline (Case 4, Fig. S3.c), E85 increased ozone relative to gasoline, but less than in Case 1. When E85 TOG emissions were increased by 38% instead of 22% relative to gasoline (Case 5, Fig. S3.d), E85 increased ozone more than in Case 1.

S3.a.

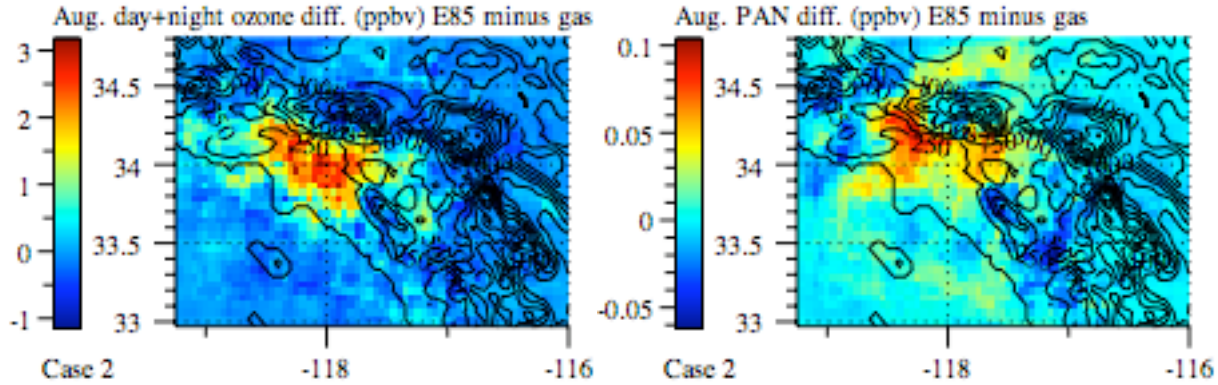

S3.b.

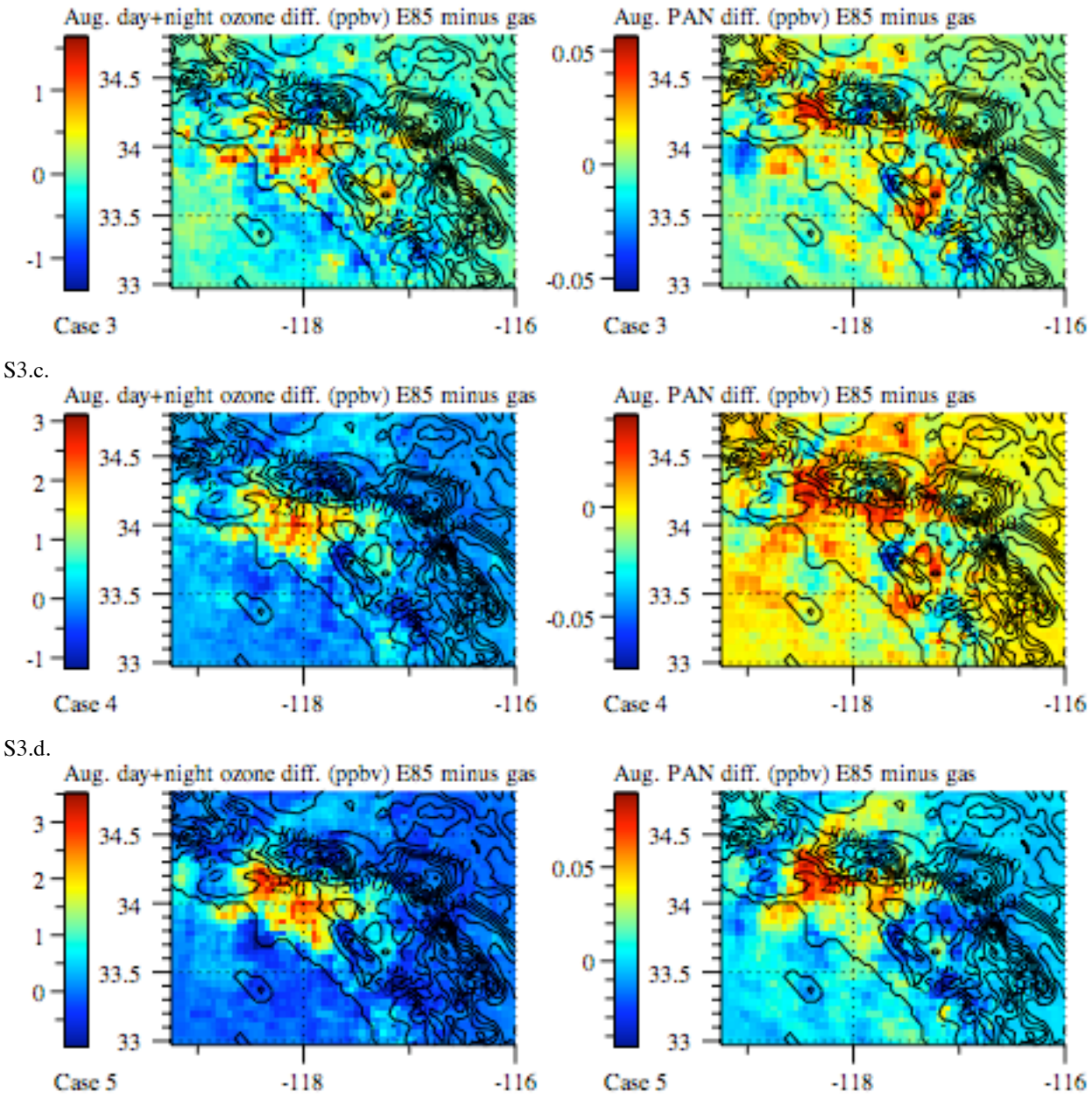

S3.c.

S3.d.

Figure S3. Differences between the E85 and gasoline simulations in the August average of 24-hour ozone and PAN, as in Fig S1 (Case 1), except (a) Case 2: NO_x-E85:NO_x-gasoline = 0.55 instead of 0.70; (b) Case 3: NO_x-E85:NO_x-gasoline = 0.85 instead of 0.70; (c) Case 4: TOG-E85:TOG-gasoline = 1.06 instead of 1.22, with the difference due to lower ethanol emissions; (d) Case 5: TOG-E85:TOG-gasoline = 1.38 instead of 1.22, with the difference due to higher ethanol emissions.

An additional sensitivity test was run to estimate the effect of converting the current (instead of 2020) Los Angeles vehicle fleet from gasoline to E85. Although such as conversion is not practical since most current gasoline vehicles cannot use E85 as a fuel, such a test provides an upper bound of the possible effects. Under this scenario, the baseline total gasoline emissions were 150% higher than those in Table 1 of the main text (e.g., the original 2002 NEI emissions were used). The percent changes in column 4 of Table 1 of the main text were then applied to the 2002 NEI emissions to obtain E85

emissions. Figure S4 shows results for this test. It indicates that the peak differences (E85 minus gasoline) in daytime ozone and 24-hour PAN were 275% and 500% higher than were those in the 2020 scenario (Figs. S1.l and S1.m, respectively). Thus, ozone and PAN differences (E85 minus gasoline) increased superlinearly with increasing baseline emissions.

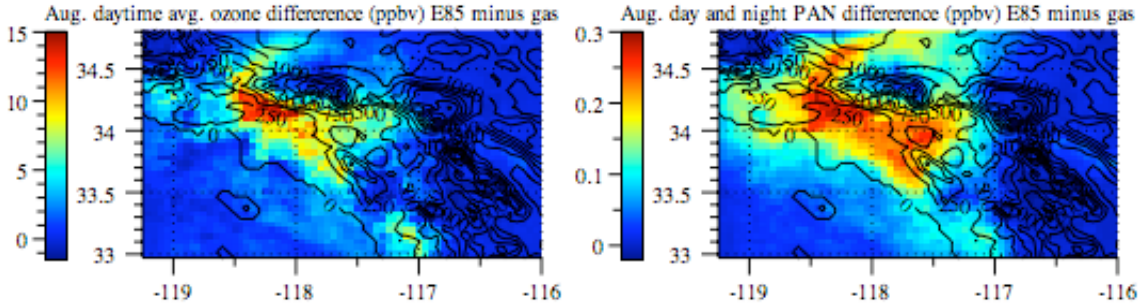

Figure S4. Modeled differences averaged over August in ozone and PAN in the Los Angeles basin when all gasoline vehicles in the basin were converted to E85 vehicles as in the Case 1 E85 simulations but with 2002 rather than 2020 emissions. These results can be compared with 2020 results in Figs. S1.l and S1.m, respectively.

Fig. S1.n shows that E85 increased peroxyacetyl nitrate (PAN), a potent eye irritant in smog and a chemical that discolors the leaves of plants. PAN increases occurred primarily in highly-populated areas. Figs. S3.a-d shows that PAN increased in the four sensitivity simulations as well with the greatest increases in Cases 2 and 5 and the least, in cases 3 and 4.

The Los Angeles basin is not heavily vegetated, but coastal regions to its north and south are and provide most of the isoprene (methyl butadiene) emissions (Fig. S1.o). Isoprene is broken down significantly by ozone; thus in locations where ozone increased, isoprene slightly decreased; in locations where ozone decreased, isoprene slightly increased (Fig. S1.o).

Ozone formation is initiated substantially by oxidation of organics by the hydroxyl radical in the presence of oxides of nitrogen and ultraviolet light. The two major methods of initializing production of the hydroxyl radical in urban air are ozone photolysis and formaldehyde photolysis. Since E85 increased ozone and formaldehyde in the basin, E85 was expected to increase the hydroxyl radical, which it did (Fig. S1.p).

The increase in the hydroxyl radical enhanced the conversion of sulfur dioxide to sulfuric acid, the subsequent condensation of sulfuric acid to aerosol S(VI) (sulfate), and the scavenging of sulfur-containing gases and aerosol particles by clouds (nucleation scavenging of aerosol particles, dissolution of sulfur dioxide and sulfuric acid into cloud drops, and aerosol-cloud coagulation). The net effect was to reduce sulfur dioxide levels (Fig. S1.q) but to increase aerosol and cloud S(VI) (primarily sulfate) concentrations (Figs. S1.r, S1.s). The increase in aerosol sulfate was accompanied by a decrease in aerosol and cloud nitrate due to reduced emission of NO_x by E85 relative to gasoline (Fig. S1.s and S1.t).

Although one study (Table 2 of the main text) found that E85 increased the emissions of particle number and mass relative to gasoline, no change in such emissions was assumed here to ensure a conservative result. As such, no effort was made to estimate the overall effect of E85 versus gasoline on particle concentrations. However, it

was found that E85 increased sulfate and low-molecular-weight secondary organic mass (ethanol, acetaldehyde, and formaldehyde dissolved in aerosol and fog water), but decreased nitrate and high-molecular-weight secondary organic aerosol mass.

3.B. Mixing Ratio Changes in the United States

Figure S5 shows August-averaged near-surface mixing ratios/concentrations from the Case 1 E85 simulation (corresponding to 2020 E85 emissions in Table S4) and the difference between the Case 1 E85 simulation and the gasoline simulation, for the United States model domain. As in Los Angeles, E85 combustion increased ethanol (Fig. S5.a), acetaldehyde (Fig. S5.b), formaldehyde (Fig. S5.c), methane (Fig. S5.d), carbon monoxide (Fig. S5.e), and molecular hydrogen (Fig. S5.f). At the same time, E85 decreased nitrogen dioxide (Fig. S5.g), 1,3-butadiene (Fig. S5.h), benzene (Fig. S5.i), toluene (not shown), and xylene (not shown).

In Los Angeles, both day/night and peak daytime ozone increased due to E85 relative to gasoline. Increases also occurred, on average, over the U.S. as a whole, but to a lesser extent on average than in Los Angeles. In some areas, such as the southeast, E85 decreased ozone, whereas in others, such as in the northeast, ozone increased, as in Los Angeles (Fig. S5.j). The main reason for the regional differences was the higher isoprene and monoterpene emissions (and mixing ratios) in the southeast relative to Los Angeles and the northeast, as shown In Fig. S5.l for isoprene and Fig. S5.m for monoterpenes. Locations of high natural biogenic organic emissions are often in the lower triangle of an ozone isopleth (Fig. S2). In this region of the isopleth, decreases in NO_x decrease ozone, whereas increases in ROGs have little impact on ozone. Although regional differences occurred in the effect of E85 on ozone, the combination of the mixing ratio changes and the population distribution (Fig. 2 of the main text) resulted in a net increase in the population-weighted mixing ratio of ozone due to E85 (Table 5 of the main text). E85 also caused regional increases and decreases in PAN mixing ratios (Fig. S5.k) but a population-weighted increase, averaged over the U.S. (Table 5 of the main text).

S5.a.

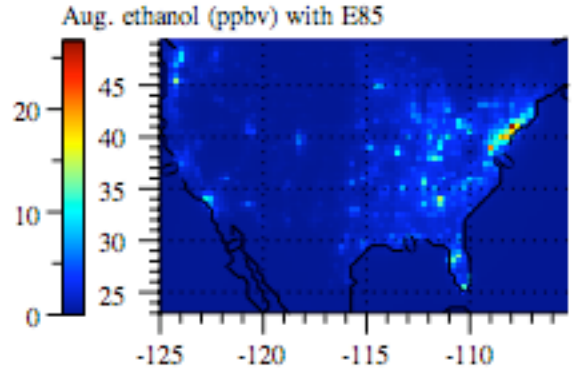

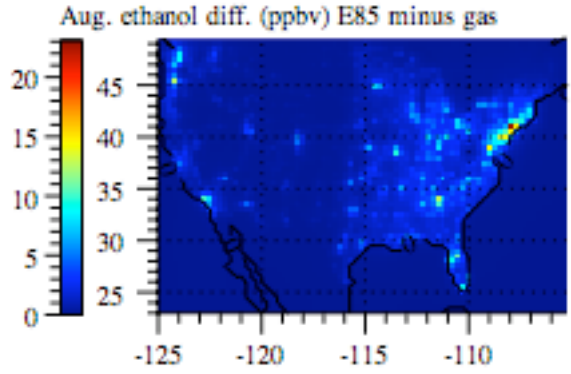

S5.b.

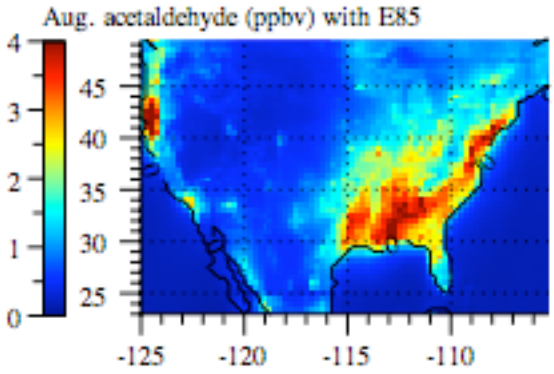

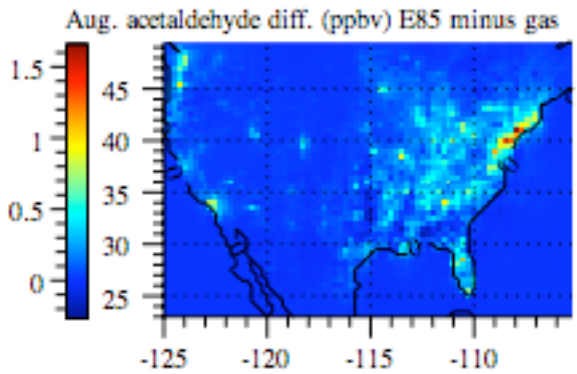

S5.c.

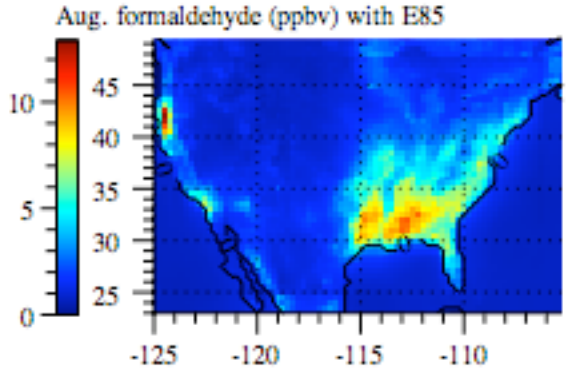

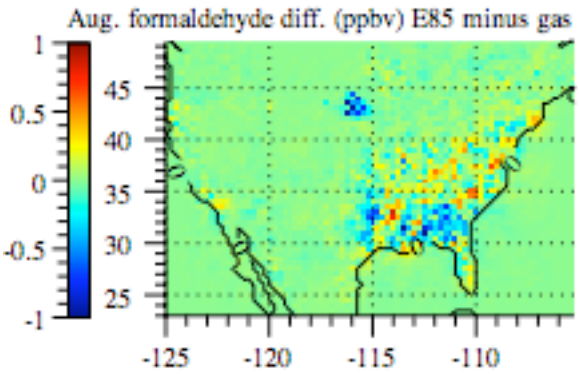

S5.d.

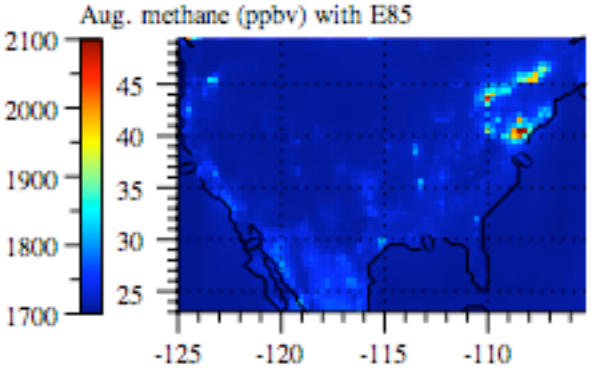

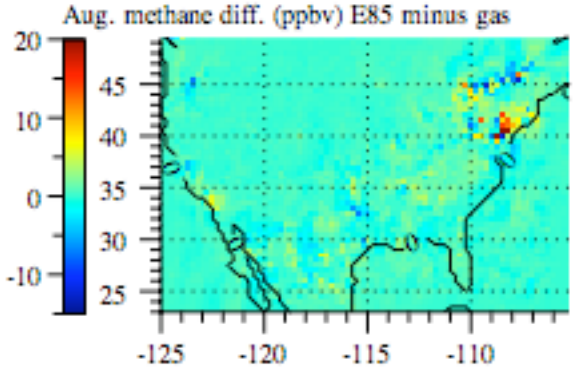

S5.e.

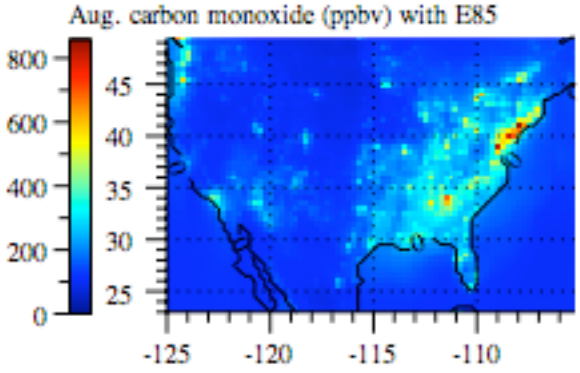

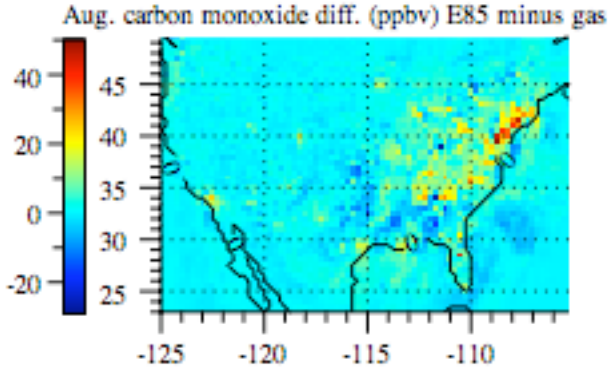

S5.f.

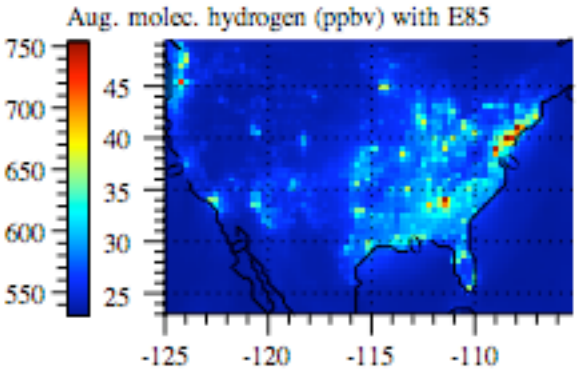

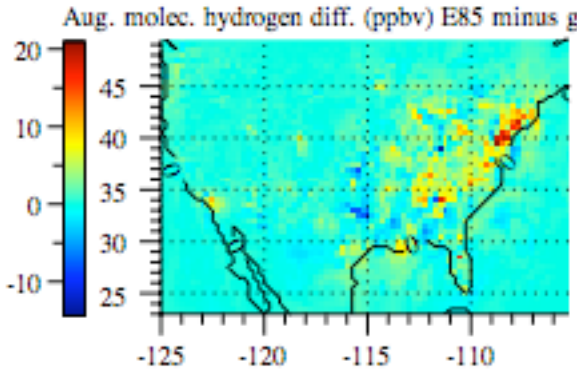

S5.g.

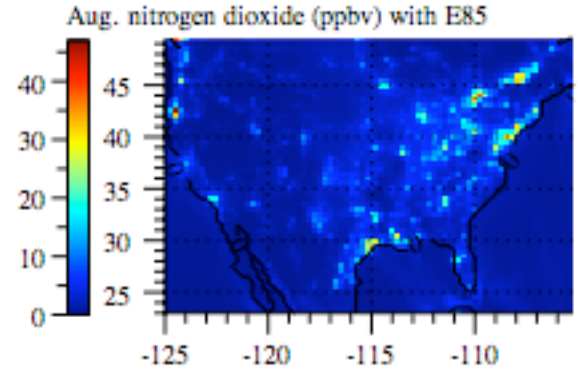

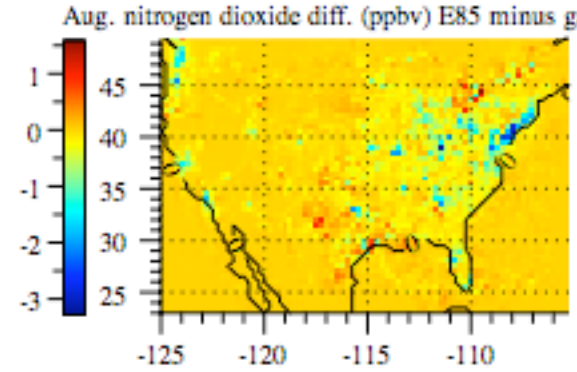

S5.h.

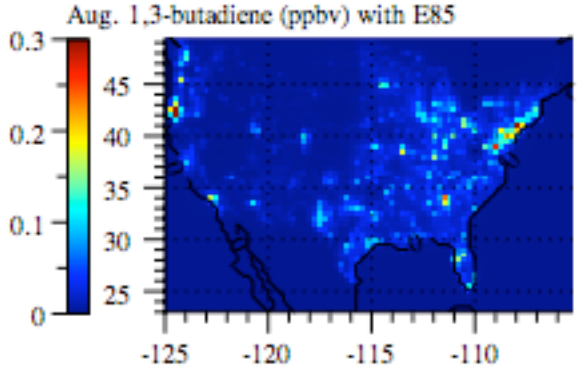

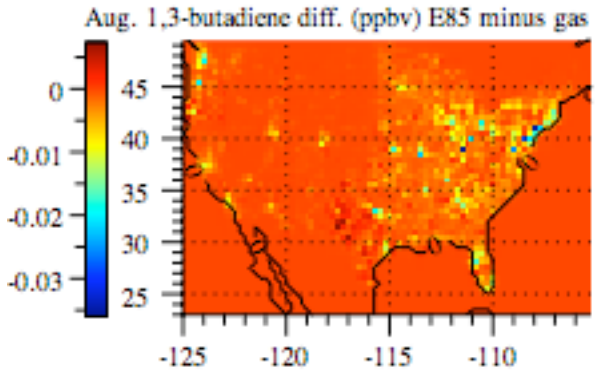

S5.i.

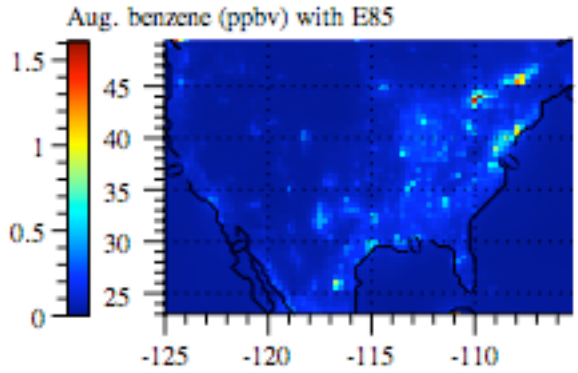

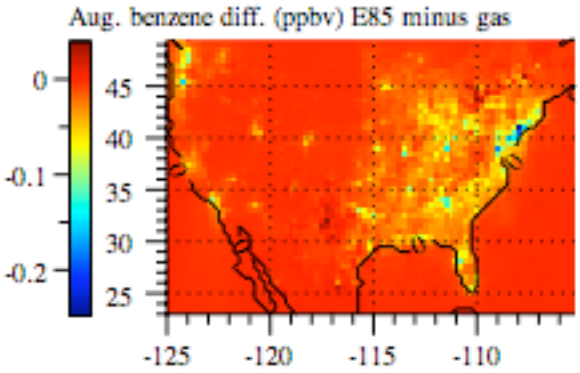

S5.j.

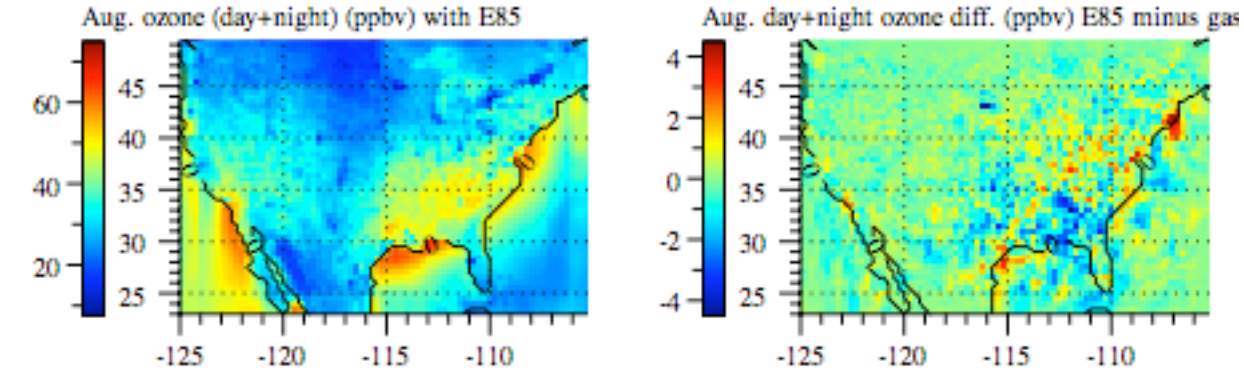

S5.k.

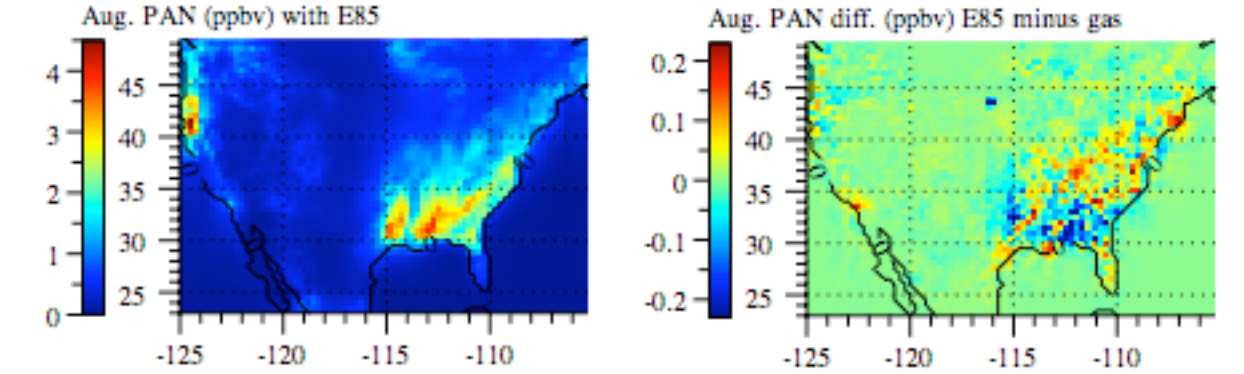

S5.l.

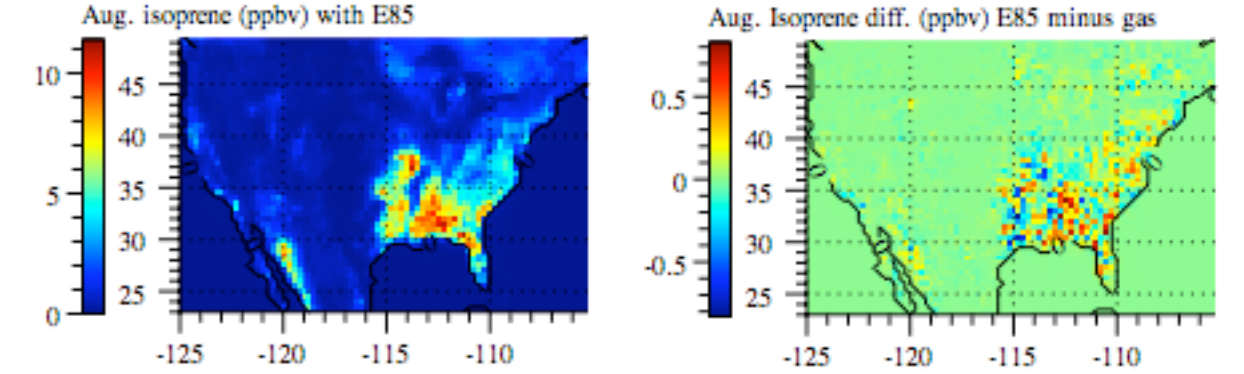

S5.m.

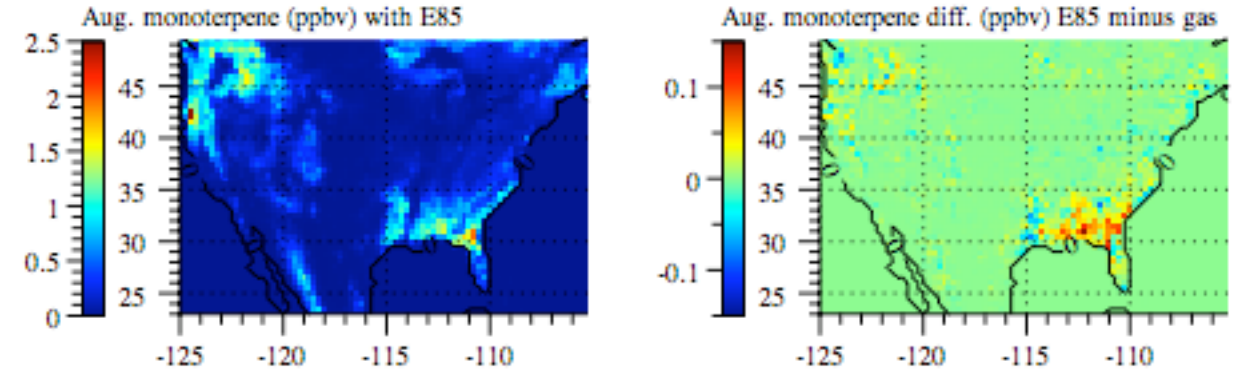

Figure S5. Same As Fig. S1, but for the U.S. as a whole.

3.C.Cancer Risk Changes in Los Angeles and the U.S.

The four major human carcinogens emitted during gasoline and E85 combustion are formaldehyde, acetaldehyde, 1,3-butadiene, and benzene. The U.S. Environmental Protection Agency (USEPA) and the California Office of Environmental Health Hazard Assessment (OEHHA) have each assigned cancer unit risk estimates (CUREs) to these chemicals. A CURE is the increased cancer risk over a 70-year average lifetime of a chemical, due to the continuous exposure to 1 $\mu g/m^3$ of the chemical.

Table S5 gives the CUREs for the four chemicals listed. The table also shows that, when these CURES were applied to emission differences between gasoline and E85 from two studies, they resulted in E85 increasing cancer-risk weighted emission by 47-58% when USEPA CUREs were used and decreasing them 31-40% when OEHHA CUREs were used, suggesting no conclusive advantage or disadvantage of E85 relative to gasoline emissions in terms of cancer risk.

Table S5. Cancer unit risk estimates (CURE) and emissions of four chemicals from gasoline and E85 vehicles, and the cancer-risk-weighted emissions of the combination of all four, derived from two studies.

	Formaldehyde	Acetaldehyde	Butadiene	Benzene	USEPA CURE-weighted emission(*)	OEHHA CURE-weighted emission(*)
EPA CURE ($m^3/\mu g$)	$1.3x10^{-5}$	$2.2x10^{-6}$	$3.0x10^{-5}$	$5.0x10^{-6}$(!)		
OEHHA CURE ($m^3/\mu g$)	$6.0x10^{-6}$	$2.7x10^{-6}$	$1.7x10^{-4}$	$2.9x10^{-5}$		
Study A[S68]						
Gasoline (mg/mi)	2.5	0.5	0.1	7.8	1.51	1.25
E85 (mg/mi)	4	18.8	0.1	3	2.22	0.86
Percent dif.					+47%	-31%
Study B [S69]						
Gasoline (mg/mi)	1.996	0.611	0.573	7.674	1.65	1.61
E85 (mg/mi)	6.695	9.343	0.499	1.682	2.61	0.96
Percent dif.					+58%	-40%

CURE=cancer unit risk estimate.

(*)The EPA or OEHHA CURE-weighted emission is the sum of the products of each individual emission and its CURE all divided by the sum of the CUREs.

(!) The EPA CURE for benzene ranges from $2.2x10^{-6}$ to $7.8x10^{-6}$. The average of these numbers was used.

Although the analysis in Table S5 is helpful, emission differences do not translate into equivalent ambient differences, since different emitted chemicals have different atmospheric reaction rates and solubilities, nor to exposure, which depends on population. In addition, some chemicals have sources aside from direct emissions. For example, acetaldehyde is produced by ethanol oxidation in the atmosphere in addition to emissions. Formaldehyde is produced by isoprene oxidation in addition to emissions.

Table 5 of the main text combines the mixing ratio changes from Figs. S1 and S5 with air density, the population distribution in Fig. 2 of the main text (scaled to 2020 population as described in the figure caption), and the CUREs from Table S5, to estimate the annual cancer risk due to E85 versus gasoline. Table 5 of the main text also shows the estimated absolute cancer risk of these pollutants from E85. The table indicates that E85 increased mortality relative to gasoline when EPA CUREs were used but decreased

mortality when OEHHA CUREs were used, an overall result consistent with that from examining cancer risk from emission changes only (Table S5). However, the change in the number of annual cancer cases was relatively small compared with the absolute cancer risk due to E85, suggesting that the cancer risk due to E85 appears similar to that of gasoline.

3.D. Ozone health risks in Los Angeles and the U.S.

In this subsection, the effects of ozone on mortality, hospitalization, and emergency-room visits is discussed. One compilation of studies found that a 10 ppbv increase in daily 1-hour maximum ozone increases total mortality in the U.S. by 0.17%-0.51%, with a central value of 0.44% (*S70*). Another found a range of 0.20%-0.60%, with a central value of 0.40% (*S71*). Here, the first range is used since it is more conservative in the upper and lower bounds. Since the health risk associated with a 100 ppbv increase in 1-hour maximum ozone roughly equals that associated with a 40 ppbv increase in 24-hour average ozone (*S70-S72*), mortality increases of 0.17%, 0.44%, and 0.51% per 10 ppbv daily 1-hour maximum ozone are roughly equivalent to 0.43%, 1.10%, and 1.28% mortality increases per 10 ppbv 24-hour average ozone. The death rate in the U.S. in 2003 was 833/yr per 100,000 (*S73*). Multiplying this by ozone mortality rates of 0.43%, 1.10%, and 1.28% per 10 ppbv 24-hour average ozone gives, 0.354, 0.916, and 1.06, respectively, deaths per year per 100,000 population per 1 ppbv increase in 24-hour average ozone. The relative risk of ozone mortality appears to increase above unity at about 35 ppbv (e.g., Fig. 2 of *S72*). This is the cutoff assumed here for mortality, hospitalization, and asthma.

U.S. hospital admissions over all ages for respiratory diseases, which include asthma and bronchitis, among others, increase by about 1.65% per 10 pbbv increase in 1-hour maximum ozone (*S70-S71*) or 4.13% per 10 ppbv increase in 24-hour average ozone. The number of U.S. hospitalizations due to any respiratory problem in 2002 was 3,353,306 (*S74*), which translates to 1189 per 100,000 that year. Combining these data gives an increase of 4.91 hospital admissions per year due to ozone-related respiratory problems per 100,000 per 1 ppbv increase in 24-hour average ozone.

The number of U.S. emergency-room (ER) visits for asthma among all ages in 1999 was 1,997,000, or 732 per 100,000 (*S75*). Studies suggest ozone increases the number of ER visits for asthma in those younger than 18 by 2.31% per 10 ppbv 1-hour maximum ozone and asthma in those older than 15 by 3.5% per 10 ppbv 1-hour maximum ozone (*S70*). Assuming a weighted average increase in ER visits for asthma over all ages of 3.2% per 10 ppbv 1-hour maximum ozone (or 8% per 10 ppbv 24-hour average ozone) gives an increase of 5.86 ER visits per year due to asthma per 100,000 population per 1 ppbv 24-hour average ozone.

Table 5 of the main text shows the effect of E85 on population-weighted ozone mixing ratio and the resulting health effects (e.g., mortality, hospitalization, emergency-room visits). The table and text suggest that E85 is estimated to increase ozone and its health effects in Los Angeles and the U.S. as a whole, but not in the southeast U.S.

In sum, the combination of computer simulations, emission data, population data, and health effects data suggest that a conversion of the U.S. fleet of gasoline vehicles to E85 vehicles may increase mortality, hospitalization, and emergency-room visits due to ozone, increase eye irritation due to PAN, yet cause little change in cancer risk. As such, future E85 use is estimated to cause an equal or greater threat to public health as future gasoline vehicle use.

10. References

S1. Jacobson, M. Z., R. Lu, R. P. Turco, and O. B. Toon, Development and application of a new air pollution modeling system. Part I: Gas-phase simulations, Atmos. Environ., 30B, 1939–1963, 1996.
S2. Jacobson, M. Z., Development and application of a new air pollution modeling system. Part II: Aerosol module structure and design, *Atmos. Environ.*, *31A*, 131-144, 1997.
S3. Jacobson, M. Z., Development and application of a new air pollution modeling system. Part III: Aerosol-phase simulations, *Atmos. Environ.*, *31A*, 587-608, 1997.
S4. Jacobson, M. Z., Studying the effects of aerosols on vertical photolysis rate coefficient and temperature profiles over an urban airshed, *J. Geophys. Res.*, *103*, 10,593-10,604, 1998.
S5. Jacobson, M. Z., Isolating nitrated and aromatic aerosols and nitrated aromatic gases as sources of ultraviolet light absorption, *J. Geophys. Res.*, *104*, 3527-3542, 1999.
S6. Jacobson, M. Z., GATOR-GCMM: A global through urban scale air pollution and weather forecast model. 1. Model design and treatment of subgrid soil, vegetation, roads, rooftops, water, sea ice, and snow., *J. Geophys. Res.*, *106*, 5385-5402, 2001.
S7. Jacobson, M. Z., GATOR-GCMM: 2. A study of day- and nighttime ozone layers aloft, ozone in national parks, and weather during the SARMAP Field Campaign, *J. Geophys. Res.*, *106*, 5403-5420, 2001.
S8. Jacobson, M. Z., Strong radiative heating due to the mixing state of black carbon in atmospheric aerosols, *Nature*, *409*, 695-697, 2001.
S9. Jacobson, M. Z., J. H. Seinfeld, G. R. Carmichael, and D.G. Streets, The effect on photochemical smog of converting the U.S. fleet of gasoline vehicles to modern diesel vehicles, *Geophys. Res. Lett.*, *31*, L02116, doi:10.1029/2003GL018448, 2004.
S10. Jacobson, M.Z., The climate response of fossil-fuel and biofuel soot, accounting for soot's feedback to snow and sea ice albedo and emissivity, *J. Geophys. Res.*, *109*, doi:10.1029/2004JD004945, 2004.
S11. Colella, W.C., M.Z. Jacobson, and D.M. Golden, Switching to a U.S. hydrogen fuel cell vehicle fleet: The resultant change in emissions, energy use, and global warming gases, *J. Power Sources, 150*, 150-181, 2005.
S12. Jacobson, M.Z., and Y.J. Kaufmann, Aerosol reduction of the wind, *Geophys. Res. Lett., 33*, L24814, doi:10.1029/2006GL027838, 2006.
S13. Arakawa, A., and V. R. Lamb, A potential enstrophy and energy conserving scheme for the shallow water equations, *Mon. Wea. Rev.*, *109*, 18-36, 1981.
S14. Lu, R., and R. P. Turco, Air pollutant transport in a coastal environment, II, Three-dimensional simulations over Los Angeles basin, *Atmos. Environ.*, *29*, 1499-1518, 1995.
S15. Walcek, C. J., and N. M. Aleksic, A simple but accurate mass conservative, peak-preserving, mixing ratio bounded advection algorithm with fortran code, *Atmos. Environ.*, *32*, 3863-3880, 1998.
S16. Jacobson, M. Z., Improvement of SMVGEAR II on vector and scalar machines through absolute error tolerance control. *Atmos. Environ., 32*, 791–796, 1998.
S17. Jacobson, M.Z., *Fundamentals of Atmospheric Modeling, Second Edition*, Cambridge University Press, New York, 813 pp., 2005.
S18. Sander, S.P., R.R. Friedl, D.M. Golden, M.J. Kurylo, G.K. Moortgat, H. Keller-Rudek, P.H. Wine, A.R. Ravishankara, C.E. Kolb, M.J. Molina, B.J. Finlayson-Pitts, R.E. Huie, and V.L. Orkin, Chemical kinetics and photochemical data for use in atmospheric studies, Evaluation Number 15, JPL Publication No. 06-2, 2006.
S19. Atkinson, R., D.L. Baulch, R.A. Cox, et al., Evaluated kinetic, photochemical, and heterogeneous data for atmospheric chemistry. Supplement V., *J. Phys. Chem. Ref. Data*, *26*, 521-1011, 1997.
S20. Gery, M. W., G.Z. Whitten, J.P. Killus, and M.C. Dodge A photochemical kinetics mechanism for urban and regional scale computer modeling. *J. Geophys. Res., 94*, 12,925-12,956, 1989; Gery, M. W., G.Z. Whitten, and J.P. Killus, Development and testing of the CBM-IV for urban and regional modeling, Rep. EPA-600/3-88-012. U. S. Environmental Protection Agency, Research Triangle Park, NC, 1988.
S21. Master Chemical Mechanism, http://mcm.leeds.ac.uk/MCM, 2006.
S22. Bahta, Int. J. Chem. Kinetics, 16, 1227-1246, 2004.
S23. Paulson, S. E. and J.H. Seinfeld, Development and evaluation of a photooxidation mechanism for isoprene. *J. Geophys. Res*, *97*, 20,703-20,715, 1992.
S24. Atkinson,R. Gas-phase troposheric chemistry of volatile organic compounds, 1, Alkanes and alkenes, J. Phys. Chem. Ref. Data, 26, 215-290, 1997.

S25 Griffin, R.J., D. Dabdub, and J.H. Seinfeld, Secondary organic aerosol 1. Atmospheric chemical mechanism for production of molecular constituents, *J. Geophys. Res., 107*, (D17), 4332, doi:10.1029/2001JD000541, 2002.

S26. Yin, F., D. Grosjean, and J.H. Seinfeld, Photooxidation of dimethyl sulfide and dimethyl disulfide. I: Mechanism development. *J. Atmos. Chem.*, *11*, 309-64, 1990.

S27. Jacobson, M. Z., Analysis of aerosol interactions with numerical techniques for solving coagulation, nucleation, condensation, dissolution, and reversible chemistry among multiple size distributions, *J. Geophys. Res.*, *107* (D19), 4366, doi:10.1029/ 2001JD002044, 2002.

S28. Jacobson, M. Z., Development of mixed-phase clouds from multiple aerosol size distributions and the effect of the clouds on aerosol removal, *J. Geophys. Res.*, *108* (D8), 4245, doi:10.1029/2002JD002691, 2003.

S29. Vehkamaki, H., M. Kulmala, I. Napari, K.E.J. Lehtinen, C. Timmreck, M. Noppel, and A. Laaksonen, An improved parameterization for sulfuric acid-water nucleation rates for tropospheric and stratospheric conditions, *J. Geophys. Res., 107* (D22), 4622, doi:10.1029/2002JD002184, 2002.

S30. Napari I., Noppel M. Vehkamaki H., and Kulmala M., Parameterization of ternary nucleation rates for H_2SO_4-NH_3-H2O vapors. *J. Geophys. Res.*, *107* (D19), 4381, doi:10.1029/2002JD002132, 2002.

S31. Jacobson, M.Z., A solution to the problem of nonequilibrium acid/base gas-particle transfer at long time step, *Aerosol Sci. Technol, 39*, 92-103, 2005.

S32. Jacobson, M. Z., Studying The effects of calcium and magnesium on size-distributed nitrate and ammonium with EQUISOLV II, *Atmos. Environ., 33*, 3635-3649, 1999.

S33. Mellor, G. L., and T. Yamada, Development of a turbulence closure model for geophysical fluid problems, *Revs. of Geophys. and Space Phys.*, *20*, 851-875, 1982.

S34. Ding, P., and D. A. Randall, A cumulus parameterization with multiple cloud-base levels, *J. Geophys. Res.*, *103*, 11,341-11,353, 1998.

S35. Toon, O. B., C. P. McKay, T. P. Ackerman, and K. Santhanam, Rapid calculation of radiative heating rates and photodissociation rates in inhomogeneous multiple scattering atmospheres, *J. Geophys. Res.*, *94,* 16,287-16,301, 1989.

S36. Jacobson, M.Z., A refined method of parameterizing absorption coefficients among multiple gases simultaneously from line-by-line data, *J. Atmos. Sci., 62*, 506-517, 2005.

S37. Toon, O. B., and T.P. Ackerman, Algorithms for the calculation of scattering by stratified spheres, *Appl. Opt. 20*, 3657-60, 1981.

S38. Grenfell, T.C., and S.G. Warren, Representation of a nonspherical ice particle by a collection of independent spheres for scattering and absorption of radiation, *J. Geophys. Res.*, *104*, 31,697-31,709, 1999.

S39. Ketefian G., and Jacobson M.Z, Development and application of a 2-D potential-enstrophy-, energy-, and mass-conserving mixed-layer ocean model with arbitrary boundaries, *Mon. Weath. Rev.*, in review, 2006.

S40. Jacobson, M.Z., Studying ocean acidification with conservative, stable numerical schemes for nonequilibrium air-ocean exchange and ocean equilibrium chemistry, *J. Geophys. Res., 110*, D07302, doi:10.1029/2004JD005220, 2005.

S41. United States Environmental Protection Agency (USEPA). Clearinghouse for Inventories and Emission Factors, http://www.epa.gov/ttn/chief/, 2006.

S42. Carter, W.P.L., Development of an improved chemical speciation database for processing emissions of volatile organic compounds for air quality models, http://pah.cert.ucr.edu/~carter/emitdb/, Aug. 30, 2005.

S43. Streets, D.G., U.S. 2030 Emission growth factors by Sector and World Region, *pers. comm.*, 2005.

S44. California Air Resources Board, Almanac Emission Project Data, www.arb.ca.gov/ei/emissiondata.htm, 2006.

S45. United States Environmental Protection Agency (USEPA). Improvements in Vegetation Cover Data, http://www.epa.gov/AMD/, 2006.

S46. United States Geological Survey (USGS) / U. Nebraska, Lincoln / European Commission's Joint Research Center 1-km resolution global landcover characteristics data base, derived from Advanced Very High Resolution Radiometer (AVHRR) data from the period April 1992 to March 1993, 1999.

S47. Guenther, A., et al., A global model of natural volatile organic compound emissions, *J. Geophys. Res.*, *100*, 8873-8892, 1995.
S48. Bond, T.C., D.G. Streets, K.F. Yarber, S.M. Nelson, J.-H. Woo, and Z. Klimont, Development of a global black carbon inventory, *J. Geophys. Res.*, 109, D14203, doi: 10.1029/2003JD003697, 2004.
S49. Corbett, J.J.; Koehler, H.W. *J. Geophys. Res., 108* (D20), 4650, doi:10.1029/2003JD003751, 2003.
S50. Jacobson, M.Z., Effects of externally-through-internally-mixed soot inclusions within clouds and precipitation on global climate, *J. Phys. Chem. A, 110*, 6860-6873, 2006.
S51. Sutkus, D.J., S.L. Baughcum, and D.P. DuBois, Scheduled Civil Aircraft Emission Inventories for 1999: Database Development and Analysis, NASA/CR-2001-211216, 2001. (available at http://gltrs.grc.nasa.gov/reports/2001/CR-2001-211216.pdf)
S52. Mortlock, A.M., and R. Van Alstyne, Military, Charter, Unreported Domestic Traffic and General Aviation: 1976, 1984, 1992, and 2015 Emission Scenarios, NASA CR- 1998-207639, 1998. (available at http://ntrs.nasa.gov/archive/nasa/casi.ntrs.nasa.gov/19980047346_1998120131.pdf)
S53. Schultz, M.G., A. Heil, J.J. Hoelzemann, A. Spessa, K. Thonicke, J. Goldammer, A. Held, J.M.C. Pereira, Global emissions from vegetation fires from 1960 to 2000, in review, 2006.
S54. Andreae, M. O., and P. Merlet, Emission of trace gases and aerosols from biomass burning, *Global Biogeochemical Cycles*, *15*, 955-966, 2001.
S55. Monahan, E. C., D. E. Spiel, and K. L. Davidson, A model of marine aerosol generation via whitecaps and wave disruption in oceanic whitecaps. In *Oceanic whitecaps and their role in air-sea exchange processes*, E. C. Monahan and G. M. Niocaill, eds., D. Reidel Publishing, Dordrecht, Holland, pp. 167-174, 1986.
S56. Smith, M.H., and N.M. Harrison, The sea spray generation function, *J. Aerosol Sci. 29*, Suppl. 1, S189-S190, 1998.
S57. Kettle, A. J. et al., A global database of sea surface dimethylsulfide (DMS) measurements and a procedure to predict sea surface DMS as a function of latitude, longitude, and month, *Global Biogeochem. Cycles*, *13*, 399-444, 1999.Krekov, G. M., Models of atmospheric aerosols, In *Aerosol Effects on Climate*, edited by S. G. Jennings, pp. 9-72, Univ. of Ariz. Press, Tucson, 1993.
S58. Marticorena, B., G. Bergametti, B. Aumont, Y. Callot, C. N'Doume, and M. Legrand, Modeling the atmospheric dust cycle. 2. Simulation of Saharan dust sources, *J. Geophys. Res.*, 102, 4387, 1997.
S59. Food and Agricultural Organization (FAO), Soil Map of the World, Land and Water Development Division, FAO, Rome, Italy, 1995.
S60. Andres, R. J., and A. D. Kasgnoc, A time-averaged inventory of subaerial volcanic sulfur emissions, *J. Geophys. Res.*, *103*, 25,251-25,261, 1998.
S61. Schultz, M.G., T. Pulles, R. Brand, M. van het Bolscher, and S.B. Dalsoren, A global data set of anthropogenic CO, NOx, and NMVOC emissions for 1960-2000, in review, 2006, http://retro.enes.org/emissions
S62. Bouwman, A. F., D. S. Lee, W. A. H. Asman, F. J. Dentener, K. W. van der Hoek, and J. G. J. Olivier, A global high-resolution emission inventory for ammonia, *Global Biogeochem. Cycles*, *11*, 561-587, 1997.
S63. Olivier, J. G. J., A. F. Bouwman, C. W. M. Van der Maas, J. J. M. Berdowski, C. Veldt, J. P. J. Bloos, A. J. H. Visschedijk, P. Y. J. Zandveld, and J. L. Haverlag, Description of EDGAR Version 2.0: A set of global emission inventories of greenhouse gases and ozone-depleting substances for all anthropogenic and most natural sources on a per country basis on 1^{o}x1^{o} grid, National Institute of Public Health and the Environment, RIVM) report no. 771060 002 / TNO-MEP report no. R96/119, 1996.
S64. Marland, G., T. A. Boden, R. J. Andres, Global, regional, and national CO_2 emissions, In Trends: A compendium of data on global change. Carbon Dioxide Information Analysis Center, Oak Ridge National Laboratory, U.S. Department of Energy, Oak Ridge, Tenn., USA, 2006.
S65. National Centers for Environmental Prediction (NCEP), 2.5 degree global final analyses, distributed by the Data Support Section, National Center for Atmospheric Research, 2003.
S66. United States Environmental Protection Agency (USEPA). AIR Data, http://www.epa.gov/air/data/, 2006.
S67. Jacobson, M.Z., *Atmosperic Pollution: History, Science, and Regulation*, Cambridge University Press, New York, 399 pp., 2002.

S68. Black, F.; Tejada, S.; Gurevich, M. Alternative fuel motor vehicle tailpipe and evaporative emissions composition and ozone potential, *JAWMA*, *48*, 578-591, 1998.
S69. Winebrake, J.J., M.Q. Wang, and D. He, Toxic emissions from mobile sources: A total fuel-cycle analysis for conventional and alternative fuel vehicles, *J. Air Waste Manage. Assoc. 51*, 1073-1086, 2001.
S70. California Air Resources Board, Quantifying the health benefits of reducing ozone exposure, http://www.arb.ca.gov/research/aaqs/ozone-rs/ch10.pdf, 2006.
S71. Ostro, B.D., H. Tran, H., and J.I. Levy, The health benefits of reduced tropospheric ozone in California, *J. Air Waste Manage Assoc, 56*, 1007-1021, 2006.
S72. Thurston, G.D., and K. Ito, Epidemiological studies of acute ozone exposures and mortality, *J. Exposure Analysis and Env. Epidemiology, 11*, 286-294, 2001.
S73. Hoyert, D.L., M.P. Heron, S.L. Murphy, and H.-C. Kung, Deaths: Final Data for 2003, National Vital Statistics Reports, Vol. 54, No. 13, http://www.cdc.gov/nchs/fastats/deaths.htm, 2006.
S74. Merrill, C.T., A. Elixhauser, U.S. Dept. of Health and Human Services, HCUP Fact Book No. 6: Hospitalization in the United States, 2002. Appendix: 2002 statistics on stays in U.S. hospitals, principal diagnosis, www.ahrq.gov/data/hcup/factbk6/factbk6e.htm, 2005.
S75. Mannino, D.M., D.M. Homa, L.J. Akinbami, J.E. Moorman, C. Gwynn, and S.C. Redd, Surveillance for asthma – United States, 1980-1999, Center for Disease Control Morbidity and Mortality Weekly Report, Surveillance Summaries 51 (SS01), 1-13, www.cdc.gov/mmwr/preview/mmwrhtml/ss5101a1.htm#tab6, 2002.